A SEMI-IMPLICIT MULTISCALE SCHEME FOR SHALLOW WATER FLOWS AT LOW FROUDE NUMBER

STEFAN VATER AND RUPERT KLEIN

Abstract. A new large time step semi-implicit multiscale method is presented for the solution of low Froude-number shallow water flows. While on small scales which are under-resolved in time the impact of source terms on the divergence of the flow is essentially balanced, on large resolved scales the scheme propagates free gravity waves with minimized diffusion. The scheme features a scale decomposition based on multigrid ideas. Two different time integrators are blended at each scale depending on the scale-dependent Courant number for gravity wave propagation. The finite-volume discretization is based on a Cartesian grid and is second order accurate. The basic properties of the method are validated by numerical tests. This development is a further step in the development of asymptotically adaptive numerical methods for the computation of large scale atmospheric flows.

1. Introduction

Modern high performance computing (HPC) hardware allows for high resolution atmospheric flow simulations, which resolve scales ranging from small convective-scale essentially anelastic flows up to large planetary scale dynamics [see e.g., 31]. Such simulations are not only demanding in terms of problem size. They also challenge the applied numerical methods, which must correctly resolve the different characteristic flow regimes arising on the different scales captured by the discretization.

An example is the influence of sound waves and the associated compressibility. These waves are usually considered to have little influence in meteorological applications, because the much slower synoptic and planetary wave patterns associated with inertia and advection are most relevant for predicting the weather. This led to so-called approximate "sound-proof" model equations [30, 27, 1, 9], which do not include the fast acoustic waves and have been quite popular to model small scale atmospheric dynamics. The situation is different for planetary-scale dynamics, where long-wave horizontally traveling acoustic modes, i.e., Lamb waves are sometimes considered non-negligible. Furthermore, there are indications that effects of compressibility affect large-scale, deep internal wave modes of the atmosphere in a non-trivial fashion [7]. These dynamics are fairly captured by another reduced model, namely the hydrostatic primitive equations (HPEs), which are widely used in current operational general circulation models (GCMs). At resolutions of only a few kilometers, however, the HPEs loose their validity due to the breakdown of the hydrostatic assumption. Therefore, at least for an accurate representation of large scale planetary-scale dynamics, the challenge arises of combining large-scale compressible flow representations with essentially sound-proof modeling of the small scale dynamics.

2010 *Mathematics Subject Classification.* 65M08, 86A10.

Keywords. shallow water equations, multiscale time integration, asymptotically adaptive numerical methods, large time steps, balanced modes.

For the mathematical study of interactions across scales, techniques from multiple-scales asymptotics [15, 22] are increasingly used. These are extensions of the classical single-scale asymptotic method (also known as regular perturbation analysis). In the latter one, a small non-dimensional parameter of the problem and a special (asymptotic) expansion of the dependent variables are employed to obtain simplified equation sets, which still account for the physical effects characteristic to the specific scale. Examples are the aforementioned anelastic and hydrostatic approximations. In multiple-scales asymptotic analysis the asymptotic expansion is generalized in that the variables artificially depend on more than one space or time scale. This enables the study of effects arising across scales. Since the asymptotic analysis directly relates a reduced model to the full compressible flow equations, it is a natural starting point for the development of numerical methods applicable to the considered singular regimes [20, 22]. In this context, the notion of "asymptotically adaptive numerical methods" was suggested in [18, 19, 23]. Such schemes should be robust, uniformly accurate, and efficient in the vicinity of certain asymptotic regimes and over a variety of relevant applications. The idea is closely related to "asymptotic preserving" (AP) schemes [see 5, and references therein].

The aim of this work is to develop such an asymptotically adaptive numerical method, which is able to correctly simulate large scale compressible flow phenomena with high resolution. In this initial attempt not the full dynamics of the atmosphere are considered. Instead, this work deals with the shallow water equations, which describe the vertically averaged motion of an incompressible fluid with a free surface. By "shallow" one refers to the small aspect ratio between the vertical depth and a typical horizontal length scale of the problem, which justifies the hydrostatic assumption, i.e., the pressure balances the weight of the fluid. However, these equations are not only a good model for representing river flow or large scale oceanic motions (such as tsunamis). While ignoring the presence of stratification, the shallow water equations incorporate the effects of gravity and can account for the earth's rotation and for bottom topography by the addition of appropriate source terms. Therefore, they are prototypical of the hydrostatic primitive equations and are often used in the development of numerical methods for atmospheric flow problems.

Due to the vertical averaging of the prognostic variables, the shallow water equations only admit external waves. However, the external gravity waves in shallow water flows are the equivalent to Lamb waves in the compressible flow equations [14]. The considered asymptotic regime consists of long-wave acoustic waves (Lamb waves) interacting with slow advection. This is equivalent to the regime of fast gravity waves moving over short range topography in the shallow water context. The additional atmospheric effect of small scale flow divergence induced by local diabatic sources is modeled here by a time dependent bottom topography. In this context, the shallow water model represents a challenging part of the development of numerical methods for the simulation of planetary scale atmospheric flows at high resolution.

The analysis of the regime of fast gravity waves moving over short range topography reveals that it essentially consists of long-wave linearized shallow water flow interacting with small scale flow balancing the influence of the rough topography (see section 2 for details and Bresch et al. [4]). Therefore, the new scheme should

- eliminate freely propagating "compressible" short-wave modes that it cannot represent accurately due to temporal under-resolution,
- represent with second-order accuracy the "slaved" dynamics of short-wave solution components induced by slow forcing or arising in the form of high-order corrections to long-wave modes, and
- minimize numerical dispersion for resolved modes.

The first and the last point address the specific numerical dispersion behavior of common second-order implicit time discretizations, which usually slow down modes with high wave numbers. While the decision which modes can be considered to be resolved is certainly subjective and depends on the application, at some point the slow down of modes with wave numbers larger than a certain value is unacceptable. These modes should be eliminated over time in a consistent way. On the other hand, long-wave modes, whose oscillation is well resolved at a fixed position, should be well approximated. The second point refers to the balanced flow on the small scale of the regime, which depends on local source terms and the coupling to the large scale dynamics.

To achieve these goals, a semi-implicit method for the nonlinear shallow water equations is combined with a multilevel approach which has successfully been applied to the linearized equations to model multiscale behavior in Vater et al. [42]. The latter enables the association of different solution components with certain spatial scales and is based on geometric multigrid ideas. Furthermore, selective to each scale, a proper discretization is applied. The approach results in a robust representation of balanced, slowly forced fast modes on the one hand, and a proper propagation of long wave gravity waves on the other hand.

The present work extends ideas of multiscale time integration for compressible flows formulated earlier in [18, 11, 29]. These authors already suggested to separate the short- and longwave components of a flow field and to propagate these components in time by different time integration schemes. However, they only allowed for two distinct discrete scales: one representing small-scale solution components and one for long-wave acoustic modes, which are separated from each other by a factor of 1/Ma, where Ma is the Mach number. In contrast, by introducing multigrid decompositions of the flow and a smooth blending of time integrators, we obtain a scheme in this work that allows for much more general data with true multiscale content. Our work extends that of [42] from linear wave propagation in one space dimension to the nonlinear shallow water equations.

This article is structured into the following parts. After the presentation of the governing equations we discuss the asymptotic regime of interest in the next section. The multiscale scheme is then described by a semi-discretization in time in section 3. In this course, we first extend a zero Froude number projection method to non-zero Froude numbers. The multilevel approach is included in the implicit correction step, which accounts for the correct propagation of gravity waves. Finally, we show the correct behavior of the method by some one-dimensional test cases in section 4 and give conclusions in section 5.

2. Governing Equations

The derivation of the shallow water equations can be found in numerous text books [e.g., 33, 37]. The case of non-stationary bottom topography was dealt with in Vater [40]. Here, only the resulting equations are presented and the peculiarities concerning time-dependent bottom topography are pointed out. Furthermore, the governing equations are analyzed in the limit of a small Froude number. Particularly, the asymptotic limit regime for long-wave shallow water waves passing over short-range topography as presented in Bresch et al. [4] is discussed under the additional assumption of bottom topography changing in time.

2.1. **Shallow water flows with time dependent bottom topography.**

The assumption of a time-dependent bottom topography, which is slightly unusual, is considered to model a source term which acts on the local flow divergence as outlined in the introduction. This generalization does neither change the terms arising in

the shallow water equations, nor does it introduce additional ones. Therefore, the governing equations in conservation form are given by

$$\begin{aligned} h_t + \nabla \cdot (h\boldsymbol{u}) &= 0 \\ (h\boldsymbol{u})_t + \nabla \cdot (h\boldsymbol{u} \circ \boldsymbol{u}) + \frac{1}{2\mathsf{Fr}^2}\nabla(h^2) &= -\frac{1}{\mathsf{Fr}^2} h \nabla b \end{aligned} \tag{1}$$

Here, $h(t, \boldsymbol{x})$ is the thickness or depth of the fluid and $\boldsymbol{u}(t, \boldsymbol{x})$ its depth-averaged horizontal velocity. $b(t, \boldsymbol{x})$ denotes the time and space-dependent bottom topography. The gradient operator ∇ is acting in the horizontal $\boldsymbol{x} = (x, y)$ plane. The "$\circ$" denotes the dyadic product of two vectors. A temporal change in bottom topography either changes the total height $H = h + b$ or introduces divergence in the momentum field, as can be seen from reformulating the continuity equation to

$$H_t + \nabla \cdot (h\boldsymbol{u}) = b_t \ . \tag{2}$$

Furthermore, a change in the gradient of b directly enters the source term of the momentum equation, leading to a potential disruption of the hydrostatic equilibrium of a previously balanced flow. System (1) is given in non-dimensional form introducing the dimensionless characteristic quantity $\mathsf{Fr} \coloneqq v_{\text{ref}}/\sqrt{g h_{\text{ref}}}$, which is known as Froude number. It defines the ratio between the characteristic flow velocity v_{ref} and the gravity wave speed $\sqrt{g h_{\text{ref}}}$ with g being the acceleration due to gravity and h_{ref} a reference fluid depth. Since we are interested in phenomena associated with the advective time scale of the fluid, we set $t_{\text{ref}} = \ell_{\text{ref}}/v_{\text{ref}}$ in the dimensional analysis and omitted mentioning of the Strouhal number.

The shallow water equations are mathematically equivalent to the Euler equations of compressible isentropic gas dynamics for an isentropic exponent of $\gamma = 2$. In this respect, the Froude number in the shallow water equations takes the role of the Mach number in the Euler equations, the latter being a measure of the compressibility of the fluid. Therefore, effects similar to compressibility can be also modeled by the shallow water equations, where the importance of the "compressibility" depends on the associated scales of fluid motion. In large scale atmospheric applications, a typical flow velocity is 10 m/s and the depth of the atmosphere is given by the pressure scale height, which is approximately 10 km. This results in a Froude number $\mathsf{Fr} \approx 0.03 \ll 1$, and the "compressibility" effects associated with the nonlinear nature of external gravity waves plays a minor role in this regime. Note, however, that the shallow water equations intrinsically model an incompressible fluid.

2.2. **Long-wave gravity waves passing over short-range topography.** The regime of particular interest can be characterized by long-wave shallow water waves traveling over rough topography. Consider a multiple-space-scale/single-time scale analysis for this regime akin to [18, 4, 24]. In addition to the space coordinate $\boldsymbol{x}$ defined by non-dimensionalization with the reference length ℓ_{ref}, a second large scale coordinate $\boldsymbol{\xi} = \mathsf{Fr}\,\boldsymbol{x}$ is introduced, which resolves the distance a gravity wave traverses on the considered time scale. For the bottom topography $b = b(t, \boldsymbol{x}, \boldsymbol{\xi})$ we allow for variations on both space scales. Then, the fluid depth and velocity are expressed in the multiple-scales expansion

$$(h, \boldsymbol{u})(t, \boldsymbol{x}; \mathsf{Fr}) = \sum_{i=0}^{N} \mathsf{Fr}^i (h, \boldsymbol{u})^{(i)}(t, \boldsymbol{x}, \boldsymbol{\xi}) + \mathcal{O}(\mathsf{Fr}^N) \ . \tag{3}$$

Note, that by using this ansatz, each spatial derivative of an asymptotic function $\varphi^{(i)}$ translates into

$$\nabla \varphi^{(i)}\big|_{\mathsf{Fr}} = \nabla_{\boldsymbol{x}} \varphi^{(i)} + \mathsf{Fr}\, \nabla_{\boldsymbol{\xi}} \varphi^{(i)} \tag{4}$$

for fixed Froude number Fr. As stated above, this regime has been also discussed in Bresch et al. [4], but without time dependent bottom topography. The leading

order system is separated into two subsystems representing the long-wave and the short-wave components of the flow. They are given by the *long-wave equations for rough topography*

$$\begin{aligned} \overline{(h\boldsymbol{u})^{(0)}}_t + \overline{h^{(0)}}\nabla_{\boldsymbol{\xi}} h^{(1)} &= \overline{h^{(2)}\nabla_{\boldsymbol{x}} h^{(0)}} \ , \\ h^{(1)}_t + \nabla_{\boldsymbol{\xi}} \cdot \overline{(h\boldsymbol{u})^{(0)}} &= 0 \end{aligned} \tag{5}$$

and the associated *balanced small scale flow*

$$\begin{aligned} \widetilde{(h\boldsymbol{u})^{(0)}}_t + \nabla_{\boldsymbol{x}} \cdot (h\boldsymbol{u} \circ \boldsymbol{u})^{(0)} + \widetilde{h^{(0)}\nabla_{\boldsymbol{x}} h^{(2)}} &= -\widetilde{h^{(0)}}\nabla_{\boldsymbol{\xi}} h^{(1)} \ , \\ \nabla_{\boldsymbol{x}} \cdot (h\boldsymbol{u})^{(0)} = \nabla_{\boldsymbol{x}} \cdot \widetilde{(h\boldsymbol{u})^{(0)}} &= \widetilde{b}_t \ . \end{aligned} \tag{6}$$

The leading order fluid depth is given by

$$h^{(0)}(t, \boldsymbol{x}, \boldsymbol{\xi}) = H^{(0)}(t) - b(t, \boldsymbol{x}, \boldsymbol{\xi}) \ ,$$

where $H^{(0)}$ is the leading order surface elevation of the fluid and $\frac{dH^{(0)}}{dt} = \overline{b}_t$. The next order of the fluid depth $h^{(1)} = h_1(t, \boldsymbol{\xi})$ is independent of $\boldsymbol{x}$. Here the overbar denotes the average of the pertinent variable in the fast coordinate, $\boldsymbol{x}$, and the tilde indicates the zero-average remainder or fluctuation.

Compared to the linear case [cf. 40] the two systems (5) and (6) are coupled. The large-scale flow is given by the linearized shallow water equations, which involve non-balanced free surface waves. It is driven by a source term arising from the small scale flow in the momentum equation. This source represents the accumulated pressure force, which results from the small-scale flow across the rough topography. In the opposite direction, large scale gradients of the fluid depth acting on the rough topography induce small scale momentum. This modifies the otherwise balanced small scale flow.

The difference to Bresch et al. [4] when considering non-stationary bottom topography is that a source term acting on the local divergence of the flow arises. It is generated by local variations in time of the bottom topography. Furthermore, the changes of the mean in b over time induce a change in the leading order surface elevation $H^{(0)}$, and the signal speed of the long-wave gravity waves is changing not only in space, but also in time.

Similar asymptotic regimes were studied in Klein [18] concerning weakly compressible flows with small-scale entropy and vorticity, in Le Maître et al. [25] for modeling ocean flows, and in the context of atmospheric circulation near the equator in Majda and Klein [28].

The asymptotic scaling for the velocity in this regime is given by $\boldsymbol{u} \sim 1$ as $\mathsf{Fr} \to 0$. For the fluid depth we have $h - h_0(t) \sim \mathsf{Fr}$ on the large scale and $h - h_0(t) \sim \mathsf{Fr}^2$ on the small scale, respectively. This scaling should be reproduced by a numerical scheme, especially when $\Delta t \gg \frac{\Delta\xi}{\sqrt{H_0}} = \frac{\mathsf{Fr}\Delta x}{\sqrt{H_0}}$, the latter corresponding to large Courant numbers with respect to gravity waves for the time integration in the present model problem.

2.3. **From zero to low Froude numbers.** To be able to extend the numerical machinery known from projection methods applied to the zero Froude number shallow water equations (also known as "Lake equations"), the shallow water equations must be cast into a similar form. To reformulate system (1), let us decompose the fluid depth into

$$h(t, \boldsymbol{x}; \mathsf{Fr}) = h_0(t, \boldsymbol{x}) + \mathsf{Fr}^2\, h'(t, \boldsymbol{x}) \tag{7}$$

with

$$h_0(t, \boldsymbol{x}) = H_0(t) - b(t, \boldsymbol{x}) \ . \tag{8}$$

Here, H_0 is the mean background total elevation, which can only change due to flow over the boundary of the domain or to a change in the mean bottom topography.

Therefore, h_0 can only change due to boundary flow or (local) change of bottom topography. The dynamics of the flow are thus given by the perturbation h' of the fluid depth. This ansatz is justified by the asymptotic analysis of the zero Froude number limit of the governing equations and we expect that $h' = \mathcal{O}(1)$ as $\mathsf{Fr} \to 0$ in the flow regimes of interest. Inserting this into the governing system, the shallow water equations can be rewritten as

$$\begin{aligned} h_t + \nabla \cdot (h\boldsymbol{u}) &= 0 \\ (h\boldsymbol{u})_t + \nabla \cdot (h\boldsymbol{u} \circ \boldsymbol{u}) + h\nabla h' &= 0 \\ h &= h_0 + \mathsf{Fr}^2\, h' \ . \end{aligned} \tag{9}$$

Compared to the zero Froude number equations, h' takes the role of $h^{(2)}$, but is no longer a Lagrange multiplier. Therefore, also the velocity no longer satisfies a strict divergence constraint. However, at low Froude numbers, these fields should be close to their zero Froude number counterparts. This is due to the mathematical equivalence of the shallow water and the Euler equations and related convergence results for the low Mach number limit of the Euler equations [e.g. 16].

3. Numerical Scheme

The numerical scheme to correctly capture the multiscale behavior of the flow is based on a semi-implicit discretization of the shallow water equations, the latter being an extension of a zero Froude-number projection method as in Vater and Klein [41]. This construction ensures that the discretization correctly approximates the limit behavior of the equations. A second ingredient is a scale-selective multilevel scheme which was previously derived for the linearized equations [42, 40]. With this addition we account for the characteristic flow behavior on the different scales resolved by the discretization.

The semi-implicit method consists of a predictor step, which solves an auxiliary hyperbolic system. This is followed by a first elliptic correction to adjust the advective flux components. A second elliptic correction accounts for the accurate propagation of gravity waves. This is where we incorporate the multilevel scheme for linearized flows. The multilevel scheme is based on two different time discretizations. A scale-wise decomposition of the flow information based on geometric multigrid ideas enables a scale-dependent blending of the two time discretizations. Here, we employ the trapezoidal rule and the BDF(2) scheme, which are both second-order accurate and need the solution of only one linear system. The trapezoidal rule, which is equivalent to the implicit midpoint rule in the linear case, conserves energy of all wave modes. While this is advantageous for long waves, it is not desirable for high-wavenumber modes, due to the unfavorable discrete dispersion relation. Backward differentiation (BDF) schemes, on the other hand, are able to filter these short wave modes in a consistent way. In the present work, only uniform time steps are considered. This simplifies the application of multistep methods, since it is not required to account for the different time step sizes. Often these methods can be generalized to variable time steps as in the case of BDF(2) [8].

Similar to the formulation of a zero Froude number projection method as in Vater and Klein [41], the semi-implicit scheme is derived by a semi-discretization in time. The discretization in space is discussed in a second step. The essential difference to the zero Froude number case is that the ansatz (7) for the fluid depth involves the introduction of local time derivatives of this quantity. This leads to the solution of two Helmholtz problems in the correction steps.

3.1. **Explicit predictor and advective flux correction.** The auxiliary system solved in the predictor step is given by

$$\begin{aligned} h_t + \nabla \cdot (h\boldsymbol{u}) &= 0 \\ (h\boldsymbol{u})_t + \nabla \cdot (h\boldsymbol{u} \circ \boldsymbol{u}) &= -(h\nabla h')^{\text{old}} \ , \end{aligned} \tag{10}$$

where the right hand side of the momentum equation is treated as a "source term" and computed from an old (known) time level. The homogeneous part of (10) is known as the "pressureless equations" [see 2, 3, 26, and references therein]. The source term is set to $(h\nabla h')^{\text{old}}(\boldsymbol{x}) \coloneqq (h\nabla h')(t^n, \boldsymbol{x})$, where $h'^{,n}$ is computed from h^n by using (7), i.e.,

$$h'^{,n} = \frac{1}{\mathsf{Fr}^2} \left(h^n - H_0^n + b^n\right) \ . \tag{11}$$

Here and in the following $h(\boldsymbol{x}, t^n)$ is abbreviated by h^n etc.

Integrating the governing equations from time level t^n to $t^{n+1} \coloneqq t^n + \Delta t$ and using the mid-point rule by evaluating the flux terms at the half-time levels $t^{n+1/2} \coloneqq t^n + \Delta t/2$ yields

$$h^{n+1} = h^n - \Delta t \big[\nabla \cdot (h\boldsymbol{u})^{n+1/2}\big] \tag{12}$$

and

$$(h\boldsymbol{u})^{n+1} = (h\boldsymbol{u})^n - \Delta t \big[\nabla \cdot (h\boldsymbol{u} \circ \boldsymbol{u})^{n+1/2} + (h\nabla h')^{n+1/2}\big] \ , \tag{13}$$

which is second-order accurate. To obtain an accurate and stable approximation of the advective flux terms, the the momentum $(h\boldsymbol{u})^{*,n+1/2}$ computed by the auxiliary system is modified by a height correction $\delta h'^{,n}_{\text{fl}}$

$$(h\boldsymbol{u})^{n+1/2} = (h\boldsymbol{u})^{*,n+1/2} - \frac{\Delta t}{2} h^n \nabla \delta h'^{,n}_{\text{fl}} \ . \tag{14}$$

Applying the divergence to this equation in combination with the height update (12) leads to an (uncritical) Helmholtz problem for $\delta h'^{,n}_{\text{fl}}$:

$$-\frac{\mathsf{Fr}^2}{\Delta t} \delta h'^{,n}_{\text{fl}} + \frac{\Delta t}{2} \nabla \cdot (h^n \nabla \delta h'^{,n}_{\text{fl}}) = \frac{H_0^{n+1} - H_0^n}{\Delta t} - \frac{b^{n+1} - b^n}{\Delta t} - \frac{h^{*,n+1} - h^n}{\Delta t} \ . \tag{15}$$

The last term on the right hand side is obtained by substituting the divergence of the auxiliary momentum through the height equation of (10). Note that for $\mathsf{Fr} = 0$ this equation becomes identical to the first correction of a projection method as in Vater and Klein [41]. Using (14), the height at the new time level as given in (12) and the advective components of the momentum flux can be computed. This leads to an intermediate momentum update defined by

$$(h\boldsymbol{u})^{**}_{\text{TR}} \coloneqq (h\boldsymbol{u})^n - \Delta t \left[\nabla \cdot (h\boldsymbol{u} \circ \boldsymbol{u})^{n+1/2} + (h\nabla h')^n\right] , \tag{16}$$

and the momentum at the new time level is obtained by

$$(h\boldsymbol{u})^{n+1} = (h\boldsymbol{u})^{**}_{\text{TR}} - \frac{\Delta t}{2} \left(\delta h^n \nabla h'^{,n} + h^{n+1/2} \nabla \delta h'^{,n}\right) \ , \tag{17}$$

where $\delta h^n \coloneqq h^{n+1} - h^n$ and $h^{n+1/2} \coloneqq \frac{1}{2}(h^n + h^{n+1})$. The terms in the brackets have still to be computed through a second correction.

3.2. **Second correction.** As discussed above, two different discretizations are derived for the second correction. One is based on the trapezoidal rule, the other one has a BDF(2)-type discretization. These two discretizations are the basis for the subsequently derived multiscale scheme. In addition we will consider the θ-scheme, which is a blended version between the implicit midpoint/trapezoidal rule and the implicit Euler method.

The trapezoidal rule applied to the height equation results in

$$\frac{1}{2} \left[\nabla \cdot (h\boldsymbol{u})^{n+1} + \nabla \cdot (h\boldsymbol{u})^n\right] = -\frac{h^{n+1} - h^n}{\Delta t} \ . \tag{18}$$

By substitution of (17) into this equation, we obtain another (uncritical) Helmholtz equation, but this time for the height update $\delta h'^{,n} = h'^{,n+1} - h'^{,n}$, which is

$$-\frac{2\mathsf{Fr}^2}{\Delta t}\delta h'^{,n} + \frac{\Delta t}{2}\nabla\cdot(\widehat{h}^{n+1/2}\nabla\delta h'^{,n}) = 2\frac{H_0^{n+1}-H_0^n}{\Delta t} - 2\frac{b^{n+1}-b^n}{\Delta t} + \nabla\cdot(h\boldsymbol{u})^n + \nabla\cdot(h\boldsymbol{u})^{**}_{\mathrm{TR}} - \frac{\Delta t}{2}\nabla\cdot(\widehat{\delta h^n}\nabla h'^{,n}) \ . \tag{19}$$

Apart from the last term on the right hand side, for $\mathsf{Fr} = 0$ this equation is again essentially equivalent to the zero Froude number case. In case of the zero Froude number projection method, this last term (without the hat over δh^n) appears in the intermediate momentum update, since there the height update is given through $H_0(t)$ and $b(t,\boldsymbol{x})$. In the low Froude number case, however, we have $\delta h^n = \delta H_0^n + \mathsf{Fr}^2\delta h'^{,n}$, which means that actually the part $\mathsf{Fr}^2\Delta t/2\nabla\cdot(\delta h'^{,n}\nabla h'^{,n})$ should be on the left hand side of the equation, modifying the solution operator. This issue is solved by using the height update known from the first correction (denoted by the hat) to compute this term. The same is true for the weight of the Laplacian in the Helmholtz operator on the left hand side, where we also apply the height obtained from the first correction. Note, that this does not modify the final momentum update (17), where the solution $\delta h'^{,n}$ of (19) must be used to determine δh^n in order to get conservation of momentum in the absence of non-trivial bottom topography.

To obtain a BDF(2)-type discretization of the second correction, the governing equations (9) are discretized by

$$h^{n+1} = \frac{4}{3}h^n - \frac{1}{3}h^{n-1} - \frac{2\Delta t}{3}\left[\nabla\cdot(h\boldsymbol{u})^{n+1}\right] \tag{20}$$

and

$$(h\boldsymbol{u})^{n+1} = \frac{4}{3}(h\boldsymbol{u})^n - \frac{1}{3}(h\boldsymbol{u})^{n-1} - \frac{2\Delta t}{3}\left[\nabla\cdot(h\boldsymbol{u}\circ\boldsymbol{u})^{n+1} + (h\nabla h')^{n+1}\right] . \tag{21}$$

Note that the advective flux component $\nabla\cdot(h\boldsymbol{u}\circ\boldsymbol{u})$ is only available at the half time level from the predictor and first correction. Since for the BDF discretization this term is needed at the full time level t^{n+1}, it is linearly extrapolated from older time levels by

$$(h\boldsymbol{u}\circ\boldsymbol{u})^{n+1} \coloneqq (h\boldsymbol{u}\circ\boldsymbol{u})^{n+1/2} + \frac{1}{2}\left((h\boldsymbol{u}\circ\boldsymbol{u})^{n+1/2} - (h\boldsymbol{u}\circ\boldsymbol{u})^{n-1/2}\right) \ . \tag{22}$$

A resulting intermediate momentum update is then given by

$$(h\boldsymbol{u})^{**}_{\mathrm{BDF2}} \coloneqq \frac{4}{3}(h\boldsymbol{u})^n - \frac{1}{3}(h\boldsymbol{u})^{n-1} - \frac{2\Delta t}{3}\left[\nabla\cdot(h\boldsymbol{u}\circ\boldsymbol{u})^{n+1} + (h\nabla h')^n\right] , \tag{23}$$

and the momentum at the new time level is computed by

$$(h\boldsymbol{u})^{n+1} = (h\boldsymbol{u})^{**}_{\mathrm{BDF2}} - \frac{2\Delta t}{3}\left(\delta h^n\nabla h'^{,n} + h^{n+1}\nabla\delta h'^{,n}\right) \ . \tag{24}$$

Similarly to the in case of the trapezoidal rule, the momentum update (24) is then combined with (20), to obtain an equation for $\delta h'^{,n}$. This leads to the (uncritical) Helmholtz problem

$$-\frac{3\mathsf{Fr}^2}{2\Delta t}\delta h'^{,n} + \frac{2\Delta t}{3}\nabla\cdot(\widehat{h}^{n+1}\nabla\delta h'^{,n}) = -\frac{\mathsf{Fr}^2}{2\Delta t}\delta h'^{,n-1} + \frac{3h_0^{n+1} - 4h_0^n + h_0^{n-1}}{2\Delta t} + \nabla\cdot(h\boldsymbol{u})^{**}_{\mathrm{BDF2}} - \frac{2\Delta t}{3}\nabla\cdot(\widehat{\delta h^n}\nabla h'^{,n}) \ , \tag{25}$$

where $h_0^n = H_0^n - b^n$. Here again, the values with the hats are approximations obtained from the height computed in the first correction. To conserve momentum in the absence of non-trivial bottom topography, also in this case the result of (25)

must be used in the final momentum update (24) for the calculation of δh^n and h^{n+1}.

In addition to the two schemes described above, we consider the so-called θ-scheme. This means that the non-convective flux term $(h\nabla h')^{n+\theta}$ in (13) is approximated at $t^n + \theta\Delta t$, and equation (18) is substituted by

$$\theta\nabla\cdot(h\boldsymbol{u})^{n+1} + (1-\theta)\nabla\cdot(h\boldsymbol{u})^{n} = -\frac{h^{n+1}-h^n}{\Delta t}\ , \quad \theta\in[0,1]\ . \tag{26}$$

For $\theta = 1$, this method becomes the implicit Euler method. While it is of second-order accuracy only for $\theta = 0.5$ (equivalent to the trapezoidal rule), the scheme usually stabilizes for $\theta \in (0.5, 1]$, since more numerical diffusion is introduced.

3.3. **Multiscale scheme.** With the introduction of the trapezoidal and the BDF(2)-based time discretizations for the second correction, all ingredients are now at hand to apply the multilevel scheme from Vater et al. [42] as part of a semi-implicit method to the fully nonlinear shallow water equations. The idea is to define direct scale dependent splittings of the fields for fluid depth and momentum, i.e.,

$$\delta h' = \sum_{\nu=0}^{\nu_M} \delta h'^{,(\nu)} \quad \text{and} \quad (h\boldsymbol{u}) = \sum_{\nu=0}^{\nu_M} (h\boldsymbol{u})^{(\nu)}\ . \tag{27}$$

Ideally, this could be a quasi-spectral or wavelet decomposition, splitting the discrete fields into (local) high wave number and low wave number components. Each scale component should be treated depending on how well it is resolved by the underlying implicit time discretization. For each scale ν we introduce a blending parameter μ_ν, which depends on the grid-CFL number associated to the scale. It is designed, such that for well resolved scales the trapezoidal rule is used, while for scales, which are under-resolved in time, it blends towards the BDF(2) scheme.

Since we do not want to solve for separate corrections on each scale, we carefully analyze the formal contribution of the two different time discretizations on each scale. With this information and the application of multigrid prolongation and restriction operators, we derive a multilevel elliptic problem, which yields the correction for our semi-implicit discretization.

By the introduction of projection operators Π_ν^h and $\Pi_\nu^{(h\boldsymbol{u})}$, which project a height or momentum field to the scale ν, the contribution for each scale shall be given by

$$\delta h'^{,(\nu)} = (\Pi_\nu^h - \Pi_{\nu-1}^h)\delta h' \quad \text{and} \quad (h\boldsymbol{u})^{(\nu)} = (\Pi_\nu^{(h\boldsymbol{u})} - \Pi_{\nu-1}^{(h\boldsymbol{u})})(h\boldsymbol{u})\ , \tag{28}$$

where we set $\Pi_{-1}^h \equiv 0$ and $\Pi_{-1}^{(h\boldsymbol{u})} \equiv 0$ for simplicity. The scale-wise contribution, which results from blending of the schemes, is then defined as follows. With the application of the two schemes for the semi-implicit solution of the shallow water equations, two different intermediate momentum updates are available after the first correction. For the trapezoidal time discretization this is (16), whereas for the BDF(2)-based discretization the update is given by (23). With these updates, the right hand sides of the second correction equations (19) and (25) are given by

$$f_{\mathrm{TR}}^{\delta h'} = -\frac{2}{\Delta t}\left[2\frac{h_0^{n+1}-h_0^n}{\Delta t} + \nabla\cdot(h\boldsymbol{u})^n + \nabla\cdot(h\boldsymbol{u})_{\mathrm{TR}}^{**} - \frac{\Delta t}{2}\nabla\cdot(\widehat{\delta h}^n\nabla h'^{,n})\right] \tag{29}$$

and

$$f_{\mathrm{BDF2}}^{\delta h'} = \frac{3\mathsf{Fr}^2}{4\Delta t^2}\delta h'^{,n-1} - \frac{3}{2\Delta t}\left[\frac{3h_0^{n+1}-4h_0^n+h_0^{n-1}}{2\Delta t} + \nabla\cdot(h\boldsymbol{u})_{\mathrm{BDF2}}^{**} - \frac{2\Delta t}{3}\nabla\cdot(\widehat{\delta h}^n\nabla h'^{,n})\right]\ . \tag{30}$$

Here, both correction equations have been normalized, such that the weighted Laplacian is essentially the same in the two resulting Helmholtz operators. Note, that

this choice is somehow arbitrary, and one could have chosen another normalization. For example in Vater et al. [42] we used a normalization where the terms without derivatives in the Helmholtz operators have the common weight 1. Further analysis revealed, however, that this choice can introduce spurious kinks into the solution for the momentum variable. The Helmholtz operators are then given by

$$A_{\mathrm{TR}} = \frac{4\mathsf{Fr}^2}{\Delta t^2}\mathrm{id} - \nabla\cdot(\widehat{h}^{n+1/2}\nabla) \quad \text{and} \quad A_{\mathrm{BDF2}} = \frac{9\mathsf{Fr}^2}{4\Delta t^2}\mathrm{id} - \nabla\cdot(\widehat{h}^{n+1/2}\nabla)\ . \tag{31}$$

Note that here we also modified the weight in the Laplacian of the operator for the BDF2 scheme from $\widehat{h}^{n+1}$ to $\widehat{h}^{n+1/2}$. Using the projections from (28), a scale-wise application and summation over the scales results in a multiscale operator, which is given by

$$A \coloneqq \sum_{\nu=0}^{\nu_M} \left(\mu_\nu A_{\mathrm{TR}} + (1-\mu_\nu)A_{\mathrm{BDF2}}\right)\left(\Pi_\nu^h - \Pi_{\nu-1}^h\right)\ , \tag{32}$$

or, in particular for the operators defined in (31)

$$A \coloneqq \frac{\mathsf{Fr}^2}{\Delta t^2}\left[\sum_{\nu=0}^{\nu_M}\left(4\mu_\nu + \tfrac{9}{4}(1-\mu_\nu)\right)\left(\Pi_\nu^h - \Pi_{\nu-1}^h\right)\right] - \nabla\cdot(\widehat{h}^{n+1/2}\nabla)\ . \tag{33}$$

With this operator the elliptic equation of the second correction for the solution of $\delta h'^{,n+1}$ becomes

$$A\,\delta h'^{,n+1} = \sum_{\nu=0}^{\nu_M}\left(\mu_\nu f_{\mathrm{TR}}^{\delta h',(\nu)} + (1-\mu_\nu) f_{\mathrm{BDF2}}^{\delta h',(\nu)}\right) \tag{34}$$

which also involves a scale dependent right hand side. With the solution of this Helmholtz problem, the momentum at the new time level is computed according to

$$(h\boldsymbol{u})^{n+1} = \sum_{\nu=0}^{\nu_M}\left(\mu_\nu (h\boldsymbol{u})_{\mathrm{TR}}^{n+1,(\nu)} + (1-\mu_\nu)(h\boldsymbol{u})_{\mathrm{BDF2}}^{n+1,(\nu)}\right)\ , \tag{35}$$

where the scale dependent contributions are computed by blending the updates that would be obtained by either the trapezoidal or the BDF(2) time discretization. They are given by projecting

$$(h\boldsymbol{u})_{\mathrm{TR}}^{n+1} = (h\boldsymbol{u})_{\mathrm{TR}}^{**} - \frac{\Delta t}{2}\left(\delta h^n \nabla h'^{,n} + h^{n+1/2}\nabla\delta h'^{,n}\right) \tag{36}$$

and

$$(h\boldsymbol{u})_{\mathrm{BDF2}}^{n+1} = (h\boldsymbol{u})_{\mathrm{BDF2}}^{**} - \frac{2\Delta t}{3}\left(\delta h^n \nabla h'^{,n} + h^{n+1}\nabla\delta h'^{,n}\right) \tag{37}$$

to each scale using the projections from (28).

It remains to define how the blending weights for each grid level are determined. As described above, we would like to apply the trapezoidal rule for scale components, which are well resolved by the discretization. For smaller scales the blending should be shifted successively to the BDF(2) scheme. Since the numerical dispersion heavily depends on the CFL-number, in an initial attempt the blending parameter is set to be a function of the grid-CFL number. For simplicity, the gravity-wave speed $c = \sqrt{h}/\mathsf{Fr}$ is estimated by the square root of the mean height divided by the global Froude number in the conducted numerical simulations. This means that the grid-CFL number is given by $\mathrm{cfl}_\nu = c\Delta t/\Delta x_\nu$, where Δx_ν is the grid spacing on the respective grid level ν. The blending parameter is then computed according to

$$\mu_\nu = \begin{cases} \min\left(1, \dfrac{\nu_M - \nu}{\lfloor \log_2 \mathrm{cfl}\rfloor}\right) & \text{if } \mathrm{cfl} \geq 2\ , \\ 1 & \text{otherwise}\ , \end{cases} \tag{38}$$

where $\lfloor\cdot\rfloor$ means rounding towards minus infinity. Thus, μ_ν is chosen such that the scheme associates the implicit trapezoidal discretization with all gravity wave modes corresponding to coarse grids with grid-CFL number $\mathrm{cfl}_\nu \leq 1$ ($\mu_\nu = 1$), while the discretization is nudged towards BDF(2) for modes living on grids with $\mathrm{cfl}_\nu > 1$ ($\mu_\nu < 1$). However, if the fine-grid-CFL number is smaller than 2, the scheme would consequently end up with using only the trapezoidal rule. This choice of blending weights has been also used in the linear case [42].

3.4. **Space discretization.** The space discretization for the semi-implicit method is essentially the same as in the zero Froude number projection method. The major differences are that for non-zero Froude numbers two Helmholtz problems must be solved instead of Poisson-type problems, and that some care needs to be taken in order to get conservation of momentum for constant bottom topography.

The scheme is solved in one space-dimension with grid cells $V_i = [x_{i-1/2}, x_{i+1/2}]$. Furthermore, a dual discretization is introduced, where each dual grid cell $\bar{V}_{i+1/2} = [x_i, x_{i+1}]$ is centered around a node $x_{i+1/2}$ of the primary grid. The whole method is discretized as a finite volume method, which has the form

$$\mathbf{U}_i^{n+1} = \mathbf{U}_i^n - \frac{\Delta t}{|V_i|}\left(\mathbf{F}_{i+1/2}^{n+1/2} - \mathbf{F}_{i-1/2}^{n+1/2}\right) + \Delta t\, \mathbf{N}_i^{n+1/2} \ . \tag{39}$$

Here, $|V_i|$ is the volume of cell V_i. $\mathbf{U}_i^n$ represents an approximation to the cell mean of the unknowns $(h, hu)^T$ in the cell V_i at time t^n, and $\mathbf{F}_{i+1/2}^{n+1/2}$ is the advective part of the numerical flux across the interface at $x_{i+1/2}$. The latter approximates the average of the advective flux contribution $(hu, hu^2)^T$ over one time step $[t^n, t^{n+1}]$. The additional non-conservative part $\mathbf{N}_i^{n+1/2}$ accounts for the gradient in surface elevation and is an approximation to $(0, -hh'_x)^T$. The equations are discretized to obtain a scheme which is in conservation form for the height equation. Conservation of momentum is only valid when no bottom topography is present. In this case, also momentum should be conserved on the discrete level. Following the above (semi-discrete) derivation of the scheme, the numerical fluxes are computed in three steps

$$\begin{aligned} \mathbf{F}_{i+1/2}^{n+1/2} &\coloneqq \mathbf{F}_{i+1/2}^{*} + \mathbf{F}_{i+1/2}^{\mathsf{MAC}} + 0 \ , \\ \mathbf{N}_{i}^{n+1/2} &\coloneqq \mathbf{N}_{i}^{*} \quad + 0 \quad + \mathbf{N}_{i}^{\mathsf{P2}} \ , \end{aligned} \tag{40}$$

which represent contributions from the predictor, the first and second correction, respectively. Note that the first correction only modifies the advective flux components, while the second correction only modifies the non-conservative part. The detailed contributions are given in the appendix. For the discretization of the bottom topography b, a piecewise linear distribution on each primary grid cell which is continuous across the interfaces is assumed. The time derivatives $b_t^{n+1/2}$ are approximated by the midpoint rule using the values at full time levels.

In the predictor step the auxiliary system (10) is solved using a Godunov-type method for hyperbolic conservation laws [39]. As mentioned above, for $\Phi = 0$ these are the pressureless equations with the "source term" $(0, -h^n h'^{,n}_x)^T$ in the momentum equation. Note, that this term involves not only the contributions from the bottom topography, but also the non-convective part of the flux function. For the integration, a semi-discretization in space with second-order reconstruction in the primitive variables and Runge-Kutta time stepping is used [32]. In particular, Heun's method is applied, which is strong stability preserving (SSP) [34, 12]. The numerical fluxes are evaluated by solving the exact Riemann problem of the pressureless equations at the cell interfaces.

In the first correction, the flux divergence of the auxiliary system is corrected, which is similar to a MAC-type projection [13, 43] in case of the zero Froude-number

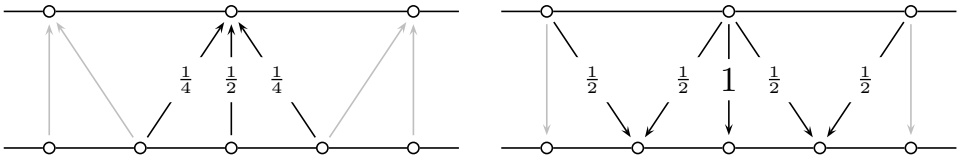

FIGURE 1. One-dimensional versions of full weighting (left) and linear interpolation (right) operators known from standard finite difference geometric multigrid. Arrows indicate mappings between grid functions associated with grid nodes.

equations. The height correction $\delta h'^{,n}_{\text{fl}}$ is continuous and piecewise linear on the dual grid, which is the 1D analogue as it was used in the solution of an elliptic problem in Süli [35], or in the first correction of the method in Vater and Klein [41] in two space dimensions. The fluid depth h^n in the weighted Laplacian of (15) is interpolated at the nodes of the primary grid by taking the average from the two neighboring cells [cf. 21].

For the second correction, the divergence on the right hand side of (19) is applied to each dual control volume. This leads to a 1D divergence defined by

$$\bar{\mathsf{D}}_{i+1/2}(u) \coloneqq \frac{1}{|\bar{V}_{i+1/2}|}\left(u_{i+1} - u_i\right) \ . \tag{41}$$

Also the computed correction $\delta h'^{,n}$ is assumed to be continuous and piecewise linear, but this time on the primary cells. Moreover, it needs to be defined how the fluid depth which enters as weight in the Laplacian on the left hand side of (19) is discretized. Here we assume that the fluid depth is piecewise constant on each cell. This leads to a piecewise constant distribution of $h(\delta h'^{,n})_x$, and the weighted Laplacian resulting from the divergence (41) is well defined.

Concerning conservation of momentum in case of flat bottom topography, it must be ensured that the term

$$hh'_x = h_0 h'_x + \mathsf{Fr}^2 h' h'_x \tag{42}$$

in the momentum equation can be written as a divergence on the discrete level. Since h_0 is constant in this case, this is no problem for the first term on the right hand side of (42). For the second term, the equality

$$h' h'_x = \frac{1}{2}((h')^2)_x \tag{43}$$

has to be achieved on the discrete level. We realize this by taking

$$(h' h'_x)_i = \left(\frac{h'_{i+1/2} + h'_{i-1/2}}{2}\right)\left(\frac{h'_{i+1/2} - h'_{i-1/2}}{\Delta x}\right) = \frac{(h'_{i+1/2})^2 - (h'_{i-1/2})^2}{2\Delta x} \ , \tag{44}$$

where the interface values are linearly interpolated from cell mean values.

The spatial discretization of the scale splitting in the second correction of the multiscale scheme is obtained by eliminating every second grid node or, equivalently, by merging two adjacent cells. In this setup the restriction and prolongation operators used in standard multigrid algorithms can be utilized to define the space decomposition. Here we use full weighting (restriction) and linear interpolation (prolongation) [36] for the fluid depth, which can be defined by a stencil. The full weighting is given by

$$R^{(\nu)} = \frac{1}{4}\begin{bmatrix} 1 & 2 & 1 \end{bmatrix} \ , \tag{45}$$

which means that a variable on the coarse grid node at grid level (ν) is derived by averaging over the values at the same node and the two adjacent nodes on the fine

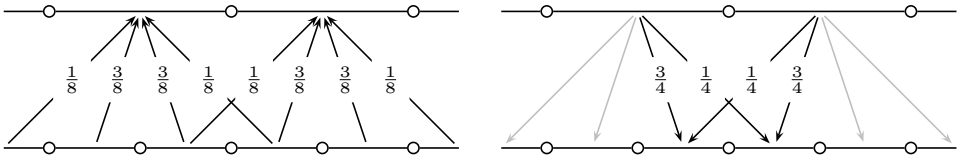

FIGURE 2. One-dimensional versions of restriction (left) and prolongation (right) operators for the momentum variable. Arrows indicate mappings between grid functions associated with grid cells (instead of with grid nodes as in figure 1).

grid at grid level $(\nu+1)$ with the weights given in the stencil above (see also figure 1, left). The linear interpolation from grid level (ν) to grid level $(\nu+1)$ is given by

$$P^{(\nu)} = \frac{1}{2}\begin{bmatrix}1 & 2 & 1\end{bmatrix} . \tag{46}$$

This means that the height at grid nodes living on the fine grid level, which have a common coarse grid node, obtain the same value as on the coarse grid. The values at grid nodes in between are computed by the average of the values of the adjacent grid nodes (figure 1, right). Note, that $P^{(\nu)}$ and $R^{(\nu)}$ are adjoint up to a scaling factor.

Since $\delta h'$ and $(h\boldsymbol{u})$ are staggered in space, the splitting in the momentum field cannot be the same as the one for the height update. Ideally, the splitting should be chosen such that only the portion of the height update associated with the grid level (ν) enters the update for the momentum on the same grid level. Revisiting equations (36) and (37) shows that only first derivatives of $\delta h'$ at different time levels enter the momentum update. Therefore, the splitting in the momentum must match the splitting in $\partial\delta h'/\partial x$ induced by the h-splitting [42]. This results in a restriction with stencil

$$\hat{R}^{(\nu)} = \frac{1}{8}\begin{bmatrix}1 & 3 & 3 & 1\end{bmatrix} \tag{47}$$

for the momentum (Figure 2, left). The obvious choice for the prolongation operator is a scaled version of the adjoint of the restriction operator $\hat{R}^{(\nu)}$, which results in

$$\hat{P}^{(\nu)} = \frac{1}{4}\begin{bmatrix}1 & 3 & 3 & 1\end{bmatrix} , \tag{48}$$

which is visualized in figure 2 (right).

A grid function φ can then be decomposed into fractions $\varphi^{(\nu)}$ associated to different grid levels using the prolongation and restriction operators $P^{(\nu)}$ and $R^{(\nu)}$. The grid function on the coarsest level is obtained by the operation

$$\varphi^{(0)} = \left(R^{(0)} \circ R^{(1)} \circ \cdots \circ R^{(\nu_M-1)}\right)\varphi , \tag{49}$$

and the grid functions on finer levels are computed by

$$\varphi^{(\nu)} = \left(I - P^{(\nu-1)} \circ R^{(\nu-1)}\right) \circ \left(R^{(\nu)} \circ R^{(\nu+1)} \circ \cdots \circ R^{(\nu_M-1)}\right)\varphi . \tag{50}$$

An application of the multiscale Helmholtz operator is then realized by decomposing the data into scales, scale-dependent weighting and rebuilding the full variable. This gives the diagonal component of the operator, which includes the multiscale information. The Laplacian part can be just computed on the finest grid level, since it does not include any multiscale information.

4. Numerical Results

Having derived the multiscale scheme for computing low Froude number shallow water flows, in this section the performance of the method is evaluated for some test cases. Besides the goal of numerically verifying the second-order accuracy of the method, its asymptotic behavior in the low Froude number regime as described in Section 2.2 is investigated.

The results of the multiscale method are compared to those obtained with the semi-implicit method using the trapezoidal rule and the BDF(2) discretization in the second correction. With the exception of the last test case, the computations for the BDF(2) and the multiscale scheme are always started with an initial first step by the trapezoidal rule. By this, enough old time step values can be provided for the BDF(2)-based scheme. As mentioned above, the blending parameter μ_ν in the multilevel scheme is computed according to (38). However, the precise values are always given for reference in each test case.

Since the presented scheme is semi-implicit, two Courant numbers [6] are considered. The Courant number concerning the maximum propagation speed of information is essentially associated with the propagation of gravity waves in the low Froude number case and denoted by $\mathrm{cfl}_{\mathrm{grav}}$. Furthermore, the Courant number concerning advective phenomena (which are mainly computed by the explicit predictor) is given by $\mathrm{cfl}_{\mathrm{adv}} \coloneqq \max_i(|u_i|)\Delta t/\Delta x$, where u_i is the velocity computed for each cell.

The linear systems for the solution of $\delta h'^{,n}_{\mathrm{fl}}$ and $\delta h'^{,n}$ are solved using a matrix-free implementation of the Bi-CGSTAB algorithm [38]. In each iteration, the Euclidean norm of the residual vector is calculated, and the algorithm is terminated when either the absolute value or the value relative to the norm of the initial residuum is less than a given tolerance. In the presented calculations, this tolerance is set to 10^{-10}.

4.1. **Weakly nonlinear gravity wave.** The first test case is set up with data, which consists of an initially smooth right running shallow water simple wave in one space dimension with flat bottom topography. Due to the nonlinearity of the governing equations, a shock develops after some time. While this is one of the most simple setups one can think of, it already reveals some interesting properties of the considered numerical schemes: by the use of the method of characteristics, the exact solution is known until the development of a shock, which is useful for a convergence study. The behavior of the different schemes towards the compressible regime can be also tested, when the exact solution eventually develops a shock. Furthermore, the evolution of long-wave gravity waves can be analyzed, which is relevant for the asymptotic regime described in Section 2.2 and similar to what was investigated for the linearized equations [cf. 42, 40].

To derive the initial conditions, let us consider the characteristic variables of the shallow water equations. These are given by [see, e.g., 10]

$$p_1 = u - 2c \quad \text{and} \quad p_2 = u + 2c \,, \tag{51}$$

where $c = \sqrt{h}/\mathsf{Fr}$ is the gravity wave speed. The definition of a background state $h_0 = 1$ leads to $c_0 = 1/\mathsf{Fr}$. Then, the initial gravity wave speed is given by

$$c = c_0 + c' = \frac{1}{\mathsf{Fr}} + c' \,. \tag{52}$$

To obtain a right running simple wave, the left running characteristic is set to $p_1 = \text{const}$. This constant is chosen to obtain a zero background flow, i.e., $p_1 = -2c_0$, which gives the initial velocity field

$$u = 2(c - c_0) = 2c' \,. \tag{53}$$

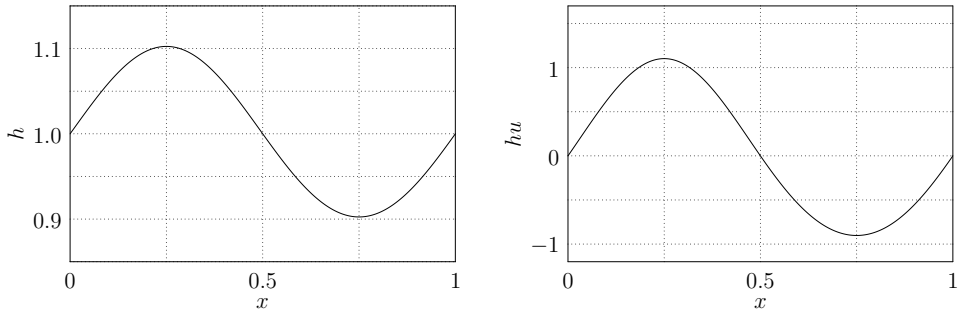

FIGURE 3. Initial conditions for the weakly nonlinear gravity wave test case with $\mathsf{Fr} = 0.1$ on a grid with 256 grid cells. Left: fluid depth, right: momentum.

Therefore, initially the local Froude number ranges from 0 to $\mathsf{Fr}_{\max} \approx \frac{u_{\max}}{c_0} = 2\,\mathsf{Fr}\max_{x\in\Omega}(c'(x))$. For the performed simulations the perturbation of the gravity wave speed is set to $c'(x) = \frac{1}{2}\sin(2\pi x)$. The computational domain is defined by the interval $\Omega = [0, 1]$ with 256 grid cells and periodic boundary conditions.

In a first setup, the Froude number is set to $\mathsf{Fr} = 0.1$ and the time step is chosen to be $\Delta t = 0.003$, which is equivalent to initial Courant numbers $\mathrm{cfl}_{\mathrm{adv}} \approx 0.77$ concerning advection and $\mathrm{cfl}_{\mathrm{grav}} \approx 8.83$ concerning the propagation of gravity waves. In Figure 3 the initial conditions for fluid depth and momentum are given. The solutions of the numerical schemes are given after 40 ($t = 0.12$) and 100 time steps ($t = 0.3$) in Figure 4. At these times the wave has traveled approximately 1.2 and 3 times, respectively, through the domain. Since a shock forms at time $t_{\mathrm{shock}} = 1/(3\pi)$, this test shows the performance of the schemes towards the compressible regime. The multiscale scheme is set up with three grid levels and blending factors $\mu_{\boldsymbol{\nu}} = (1, 1/2, 0)$.

In addition we present results for the θ-scheme with $\theta = 0.7$ and another variant of the multiscale scheme where we switch between the trapezoidal rule and the implicit Euler method (θ-scheme with $\theta = 1$). For the latter we choose six grid levels with blending factors $\mu_{\boldsymbol{\nu}} = (1, 1/2, 0, 0, 0, 0)$. Note, that this choice is different from what one would obtain using (38).

As one can see in Figure 4, for $t = 0.12$ the trapezoidal rule and multiscale scheme develop an artificial overshot in the vicinity of the shock, which continuously grows until either the time step has to be reduced or the schemes become unstable (which already happens before the time $t = 0.3$). Since the initial data only consists of long-wave information, and the contributions on the smaller scales are only small corrections, the results for both schemes are almost identical. On the other hand, the θ-scheme does not show this behavior, and the discontinuity is smeared out by numerical diffusion. The BDF(2)-based scheme shows a behavior which is in between these two extrema. To show that the multiscale scheme can also be used to suppress the spurious overshot, we have implemented the version of the multiscale scheme where we switch between the trapezoidal rule and the implicit Euler. In this case, high wave numbers are diffused by the first-order method, while the long-wave components are preserved.

The described behavior becomes even more evident at the later time $t = 0.3$, where we only show the BDF(2), the θ-scheme and the multiscale trapezoidal/implicit Euler scheme, due to the stability problem of the trapezoidal rule. Additionally, all schemes introduce a dispersive error in that they slow down the speed of the simple wave.

To test the evolution of long-wave gravity waves the Froude number is reduced to $\mathsf{Fr} = 0.02$ in a second setup. This further decreases the nonlinearity of the equations

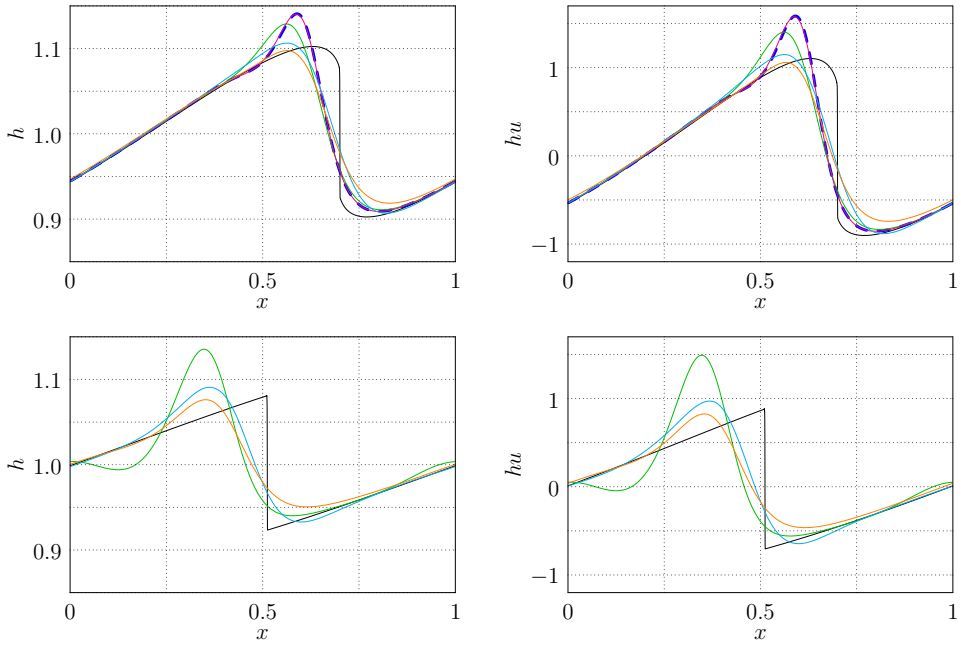

FIGURE 4. Solution of the weakly nonlinear gravity wave test case with $\mathsf{Fr} = 0.1$ at times $t = 0.12$ (top) and $t = 0.3$ (bottom) computed with $\mathrm{cfl}_{\mathrm{grav}} \approx 8.83$ on a grid with 256 grid cells. Black: exact solution, blue dashed: trapezoidal rule, green: BDF(2)-type discretization, orange: off-centered scheme ($\theta = 0.7$), magenta: multiscale trapezoidal/BDF2 scheme, cyan: multiscale trapezoidal/implicit Euler scheme. Note, that the trapezoidal rule and the multiscale trapezoidal/BDF2 schemes are only shown for $t = 0.12$.

compared to the case with $\mathsf{Fr} = 0.1$. However, due to the configuration of the initial data, the shock develops at the same time $t_{\mathrm{shock}} = 1/(3\pi)$ as before. The initial conditions for this test case are shown in Figure 5 (top). The time step is again $\Delta t = 0.003$, which is equivalent to initial Courant numbers $\mathrm{cfl}_{\mathrm{adv}} \approx 0.77$ and $\mathrm{cfl}_{\mathrm{grav}} \approx 39.55$. The solution at time $t = 0.024$ is displayed in Figure 5 (bottom). At this time, the gravity wave has traveled approximately 1.2 times through the domain, and its shape has not yet been much distorted compared to the initial data. For this test, the multiscale scheme is applied with six levels and blending parameters $\mu_{\boldsymbol{\nu}} = (1, 4/5, 3/5, 2/5, 1/5, 0)$.

At the final time the trapezoidal rule and the multiscale scheme show the smallest error in amplitude and phase compared to the exact solution. Also in this case the solutions of these schemes are nearly identical. The worst results are produced by the off-centered scheme, which has the biggest phase and amplitude errors. The method with BDF(2) in the second correction produces results which are in between these two extrema.

4.2. **Convergence in one space dimension.** The same initial conditions of a right running gravity simple wave and for $\mathsf{Fr} = 0.1$ are used in order to undertake a convergence analysis. The solution of the numerical schemes is computed on different grids and compared to the exact solution at time $t_{\mathrm{end}} = 0.05$. At this time no shock has developed yet, and the true solution can be computed using the method of characteristics. The numerical solution is computed on grids with 256, 512, 1024 and 2048 cells, and the respective time steps are given by $\Delta t_{256} = 1/320$,

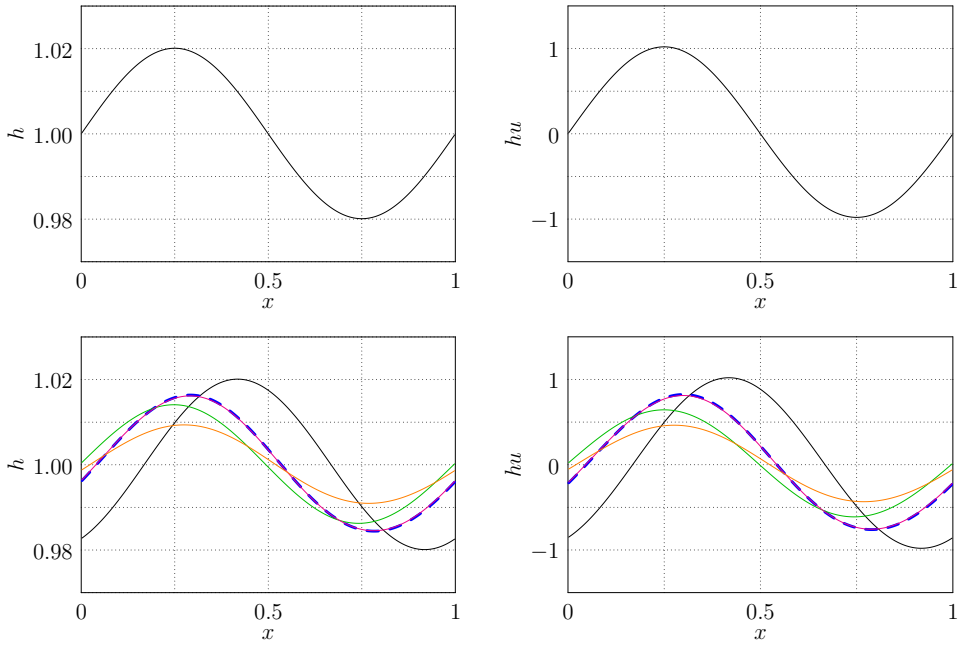

FIGURE 5. Weakly nonlinear gravity wave test case with $\mathsf{Fr} = 0.02$ computed with $\mathrm{cfl}_{\mathrm{grav}} \approx 39.55$ on a grid with 256 grid cells. Initial conditions (top). Solution at $t = 0.024$ (bottom). Black: exact solution, blue dashed: trapezoidal rule, green: BDF(2)-type discretization, orange: off-centered scheme ($\theta = 0.7$), magenta: multiscale scheme.

$\Delta t_{512} = 1/640$, $\Delta t_{1024} = 1/1280$ and $\Delta t_{2048} = 1/2560$. This corresponds to an advective Courant number $\mathrm{cfl}_{\mathrm{adv}} = 0.8$. For the multiscale method, five grid levels with $\mu_{\boldsymbol{\nu}} = (1, 1, 2/3, 1/3, 0)$ are used.

For the computation of errors and the convergence rate the error vectors $\boldsymbol{e}^N$ in fluid depth and momentum are calculated. For the latter it has elements

$$e_i^N \coloneqq (hu)_i(t_N) - (hu)_i^N \tag{54}$$

where the cell mean values of the exact solution are compared with those of the simulated data. The global error is measured using discrete versions of the L^2 and the L^∞ norms. These are defined by

$$\left\|\boldsymbol{e}^N\right\|_2 \coloneqq \left(\sum_i |V_i|\,|e_i^N|^2\right)^{1/2} \quad \text{and} \quad \left\|\boldsymbol{e}^N\right\|_\infty \coloneqq \max_i\{e_i^N\}\ . \tag{55}$$

The experimental convergence rate γ is calculated by the formula

$$\gamma \coloneqq \frac{\log(\|\boldsymbol{e}_c^N\|/\|\boldsymbol{e}_f^N\|)}{\log(\Delta x_c/\Delta x_f)}\ . \tag{56}$$

In this definition, $\boldsymbol{e}_c^N$ and $\boldsymbol{e}_f^N$ are the computed error vectors of the solution on a coarse and a fine grid and Δx_c and Δx_f are the corresponding grid spacings.

The error of the numerical solutions in the L^∞ norm is summarized in Figure 6. Furthermore, the precise values in the L^2 and L^∞ norms are given in the Appendix in Tables 1 and 2, where also the convergence rates γ between the grid levels are calculated. On fixed grids, the scheme with trapezoidal discretization in the second correction produces the smallest errors. The method with a BDF(2)-based second

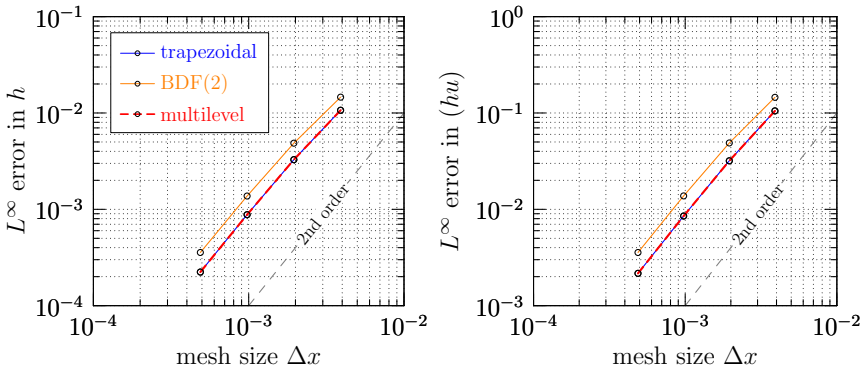

FIGURE 6. Convergence for the one-dimensional simple wave test case. L^∞ errors in h and (hu) for the different variants of the semi-implicit method.

correction produces errors, which are about 1.5 times larger. The multiscale scheme produces errors, which are comparable with those from the trapezoidal rule. This is again due to the long-wave nature of the initial conditions. As given by the values of μ_ν, only the finest scales the BDF(2)-based method is applied, which means that the calculations are nearly identical up to small deviations. The experimental convergence rates suggest for all schemes second-order accuracy.

4.3. **Balanced modes in presence of time dependent bottom topography.** In a final test case, the schemes are tested for their ability to relax to non-trivial balanced states in the presence of bottom topography varying in time. In order to do so, a test case from Vater et al. [42] [see also 40] for the linearized equations is extended to the fully nonlinear shallow water equations. The test is defined in one space dimension on the domain $\Omega = [0, 100]$. The bottom topography is given by

$$b(t,x) = \frac{\mathsf{Fr}}{\omega} \sin(\omega t)\ \tilde{q}(x - x_0)\ , \tag{57}$$

where

$$\tilde{q}(x) = \left[\frac{2\sigma^2 + \lambda^2\sigma^4 - 4x^2}{\lambda^2\sigma^4} \sin(\lambda x) + \frac{4x}{\lambda\sigma^2} \cos(\lambda x)\right] \exp\left(-\left(\frac{x}{\sigma}\right)^2\right)\ . \tag{58}$$

This means that the term $b_t(t,x) = \mathsf{Fr} \cos(\omega t)\ \tilde{q}(x - x_0)$ must be balanced by the production of local divergence. The parameters are given by $\omega = 0.2\pi$, $x_0 = 50$, $\sigma = 10$ and $\lambda = 0.32\pi$. Initially the fluid is at rest ($u \equiv 0$) with fluid depth $h \equiv 1$. When the flow is in balance, the findings from Section 2 imply that for small Froude numbers the perturbations in fluid depth and momentum should be also small, and the dynamics primarily happen in the linear regime. This means that the solution is essentially governed by the asymptotic solution obtained for the linearized shallow water equations. Translated to the given initial value problem and bottom topography, the asymptotic solutions of the perturbation in fluid depth and the velocity are

$$H_{\text{asy}}(t,x) - H_0 = -\frac{\mathsf{Fr}^3}{H_0} \omega \sin(\omega t)\ \tilde{h}(x - x_0) \tag{59}$$

with $\tilde{h}(x) = \lambda^{-2} \sin(\lambda x) \exp(-(x/\sigma)^2)$, and

$$u_{\text{asy}}(t,x) = \frac{\mathsf{Fr}}{H_0} \cos(\omega t)\ \tilde{u}(x - x_0)\ , \tag{60}$$

where $\tilde{u}(x) = [2x(\sigma\lambda)^{-2} \sin(\lambda x) - \lambda^{-1} \cos(\lambda x)] \exp(-(x/\sigma)^2)$.

In the presented computations, the Froude number is set to $\mathsf{Fr} = 0.01$ and the total background height is $H_0 = 1$. The computational grid has 256 grid cells, and the fixed time step is given by $\Delta t = 0.24$, which corresponds to an advective Courant number $\mathrm{cfl}_{\mathrm{adv}} \approx 0.006$ when the flow is essentially balanced. The Courant number corresponding to the transport of gravity waves is $\mathrm{cfl}_{\mathrm{grav}} \approx 61$.

For this test case the BDF(2)-based computations are not initialized with an initial step by the trapezoidal rule. Instead, the required state at $t^{-1} = -0.24$ is set to the balanced solution with flat bottom topography. However, compared to an initialization using the trapezoidal rule the findings are qualitatively the same. For the multiscale method six grid levels are used with a scale-dependent blending given by $\mu_{\boldsymbol{\nu}} = (1, 4/5, 3/5, 2/5, 1/5, 0)$.

Given the above initial conditions for $t = 0$, the fluid depth is in balance with the initial bottom topography. However, the temporal change of the latter introduces divergence into the velocity field, which, in turn, results in higher-order perturbations in the fluid depth. In Figure 7, the numerical results are displayed together with the asymptotic solution for the first six time steps using the trapezoidal rule and BDF(2)-based discretization. Using the trapezoidal rule, both, the computed perturbations in the fluid depth and the momentum field oscillate around the balanced state, but they do not relax to it. Additionally, the amplitude of the numerically calculated perturbations in the fluid depth are about 8 times larger compared to the asymptotic solution. The BDF(2)-based discretization results in a completely different behavior. Here, the initial deviations from the balanced state vanish after only a few time steps. After the fourth time step the numerical solution is nearly indistinguishable from the asymptotic solution. This behavior is also reproduced by the multiscale method, for which the results are given in Figure 8. These results are in good agreement with the findings for the linearized shallow water equations [42, 40].

In a second run, the simulation is started at $t = 0.15$, and the bottom topography is assumed to be flat before this time. At this time, when the bottom topography switches instantaneously to another state, both, fluid depth and momentum are not in balance. This leads to much bigger initial deviations from the asymptotic solution, as can be seen in Figure 9 for the trapezoidal rule and the BDF(2)-type discretization (note the different scaling in the y-axis for the perturbation in fluid depth for the first four time steps). To evaluate the long-term behavior, the numerical solution is additionally plotted for the time steps 35 and 36. Also in this case the solution of the trapezoidal rule does not relax to the balanced state, but rather oscillates around it. Only the long-wave perturbations are diminished with time. Here, the perturbations in fluid depth computed by the numerical scheme are about two orders of magnitude larger than those predicted by the asymptotic solution. For the momentum, the amplitude of the numerical solution is also about three times larger than the predicted balanced state.

The BDF(2)-based method, on the other hand, shows a behavior similar to the first setup. After initial deviations, which are of the same order as for the trapezoidal rule, the numerical solutions essentially relax to the balanced state predicted by the asymptotic solution. Only in the fluid depth, very high-wave-number small-amplitude deviations persist. Additional tests (not shown) suggest that these artifacts are due to the fact that the explicit predictor cannot cope with too high-wave-number modes at these large Courant numbers. In this part of the scheme, a two-stage Runge-Kutta method is used for the time discretization. Since the gravity waves are generated by the "source term" of the predictor, which is always evaluated at the old time level, high-wave-number gravity waves get very much distorted in the second stage of the Runge-Kutta scheme. This can eventually lead to instabilities, if these parts of the solution become to large.

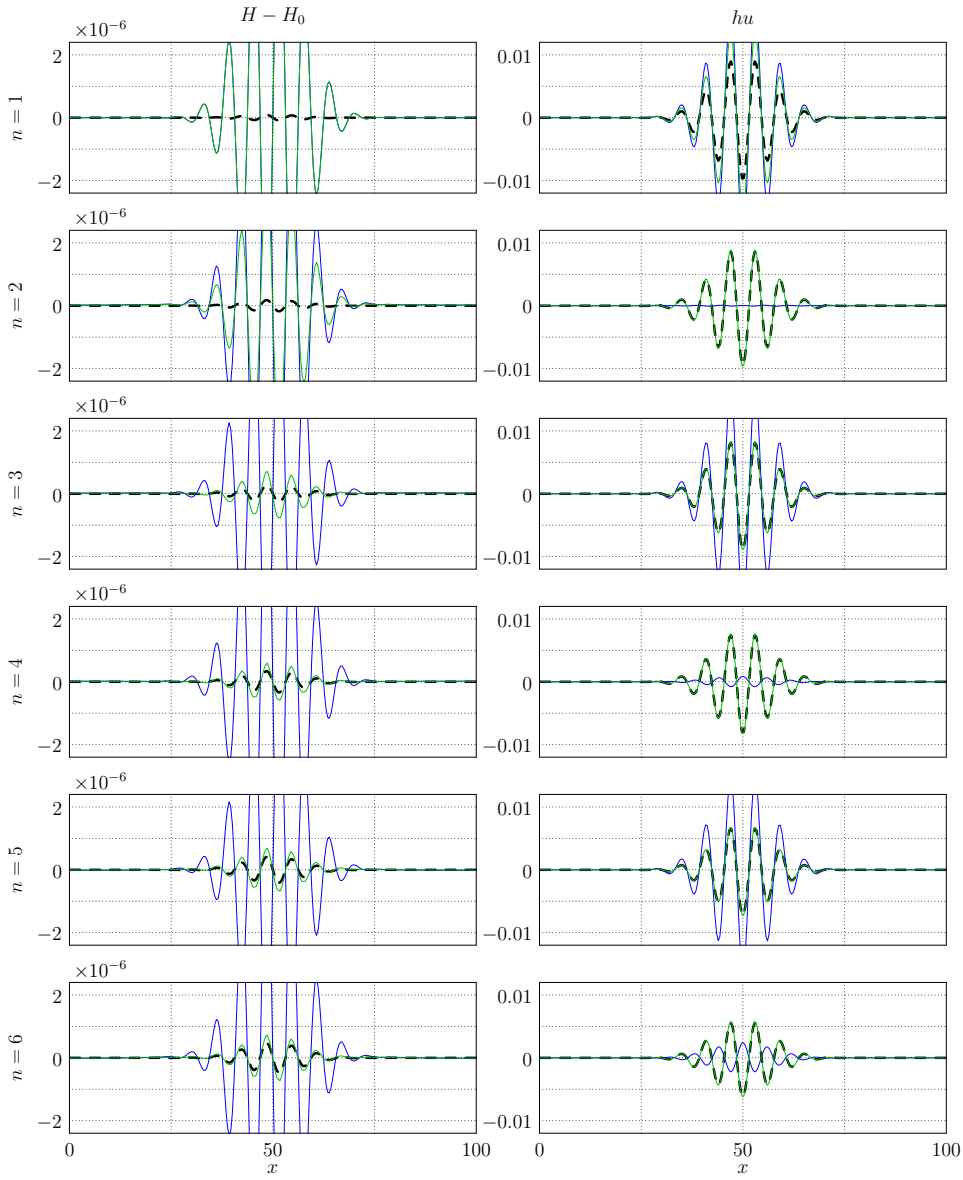

FIGURE 7. Numerical solution of the balancing test case after the first six time steps using the trapezoidal rule (blue line) and the BDF(2) scheme (green) on a grid with 256 cells, $\mathsf{Fr} = 0.01$. Left column: perturbation in fluid depth, right column: momentum. Each step n is one row. Asymptotic solution is plotted as dashed lines.

The results of the multiscale method are given in Figure 10. Qualitatively, the behavior is similar to the BDF(2)-based second correction. However, the scale dependent blending of the two methods leads to even larger very high-wave-number deviations, but whose amplitude is of the order of the perturbations in fluid depth. Also some long wave perturbations persist, which cannot propagate away due to the periodic boundary conditions.

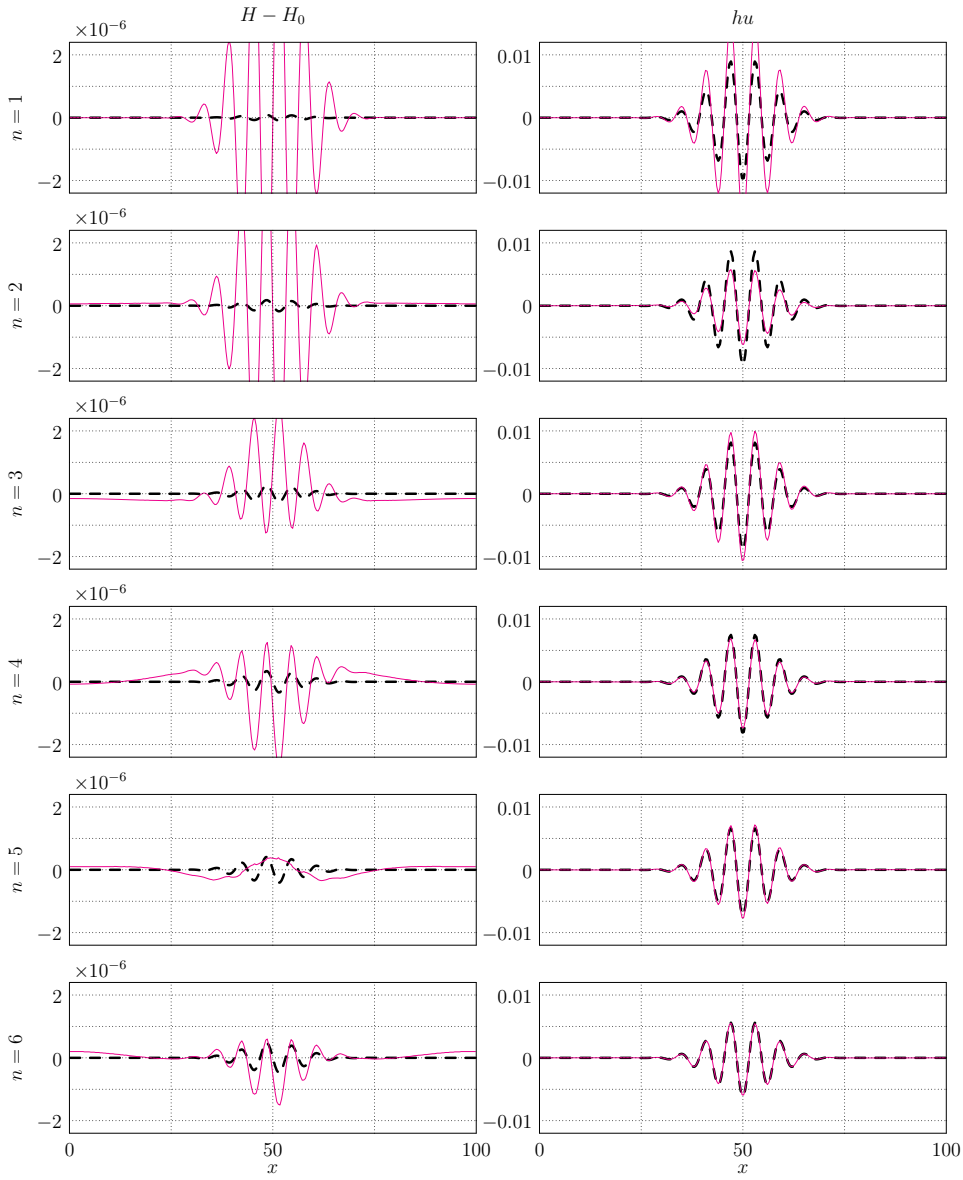

FIGURE 8. Same as Figure 7, but using the multiscale scheme (magenta).

5. Conclusion

In this work, a new multiscale semi-implicit method for the numerical solution of low Froude number shallow water flows is introduced. It is motivated by significant shortcomings of classical semi-implicit large time step integration schemes applied in current atmospheric codes. A principal feature of the new method is the diverse treatment of long and short wave solution components in accordance with the asymptotic regime of fast gravity waves traveling over short-range topography. This is achieved through a multilevel approach borrowing ideas from multigrid schemes for elliptic equations. The scheme is second-order accurate and admits time steps depending essentially on the flow velocity.

The multiscale scheme is able to properly propagate long-wave gravity waves, and their dispersion and amplitude errors are minimized as much as the considered base

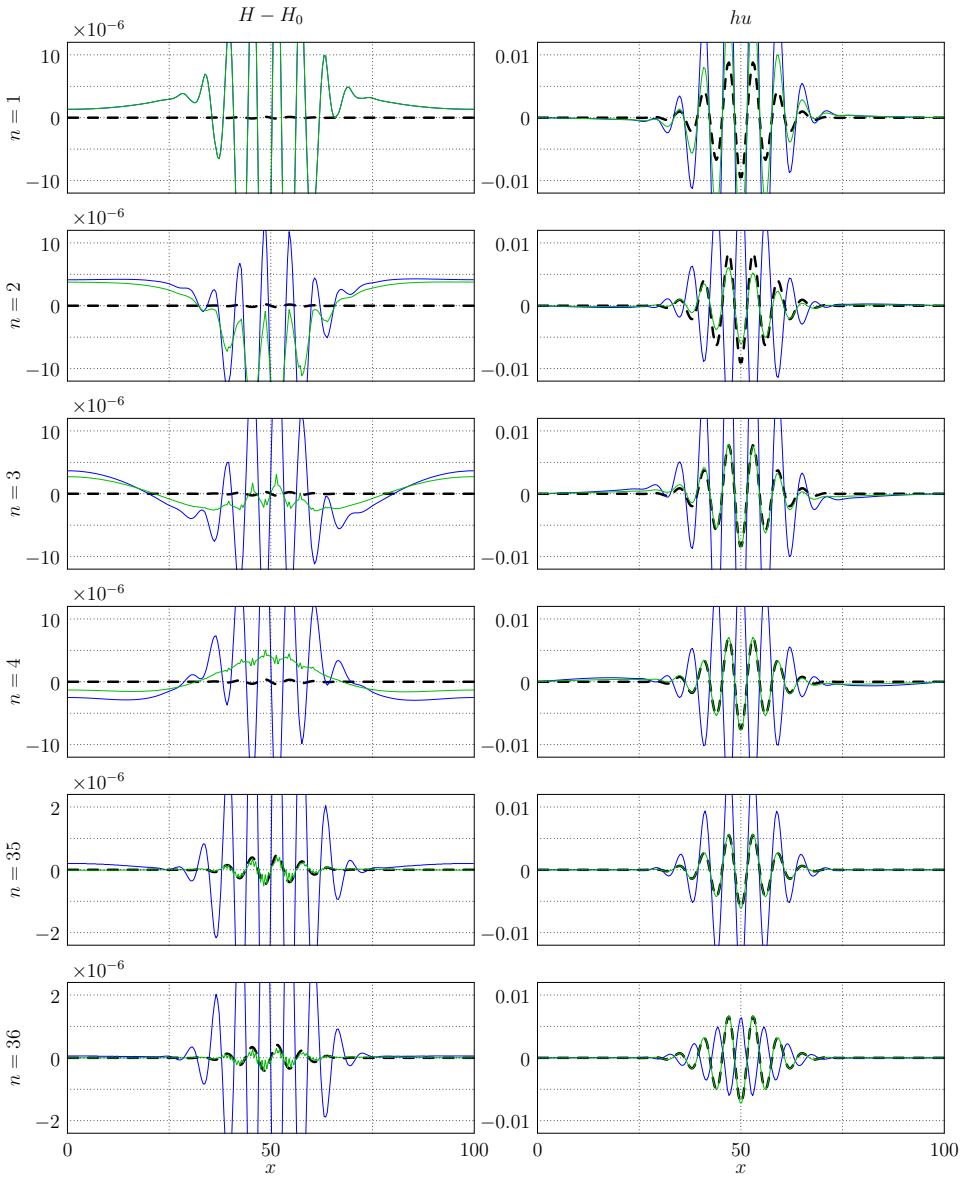

FIGURE 9. Numerical solution of the balancing test case using completely unbalanced initial data after the first four time steps and time steps 35 and 36 using the trapezoidal rule (blue line) and the BDF(2) discretization (green) on a grid with 256 cells, $\mathsf{Fr} = 0.01$. Asymptotic solution is plotted as dashed lines.

schemes admit. However, some artifacts can be observed in the fluid depth, which are probably related to the explicit predictor of the semi-implicit method. But these should be acceptable in practical applications. In the presence of bottom topography, which varies slowly in time, the balanced state is attained after a reasonable number of time steps.

The ultimate goal of this work is to develop a multiscale–multiply blended scheme that not only accounts for the scale dependent propagation properties of the various wave modes in the atmosphere, thereby creating the numerical analogon of the blended model formulation of Klein and Benacchio [17].

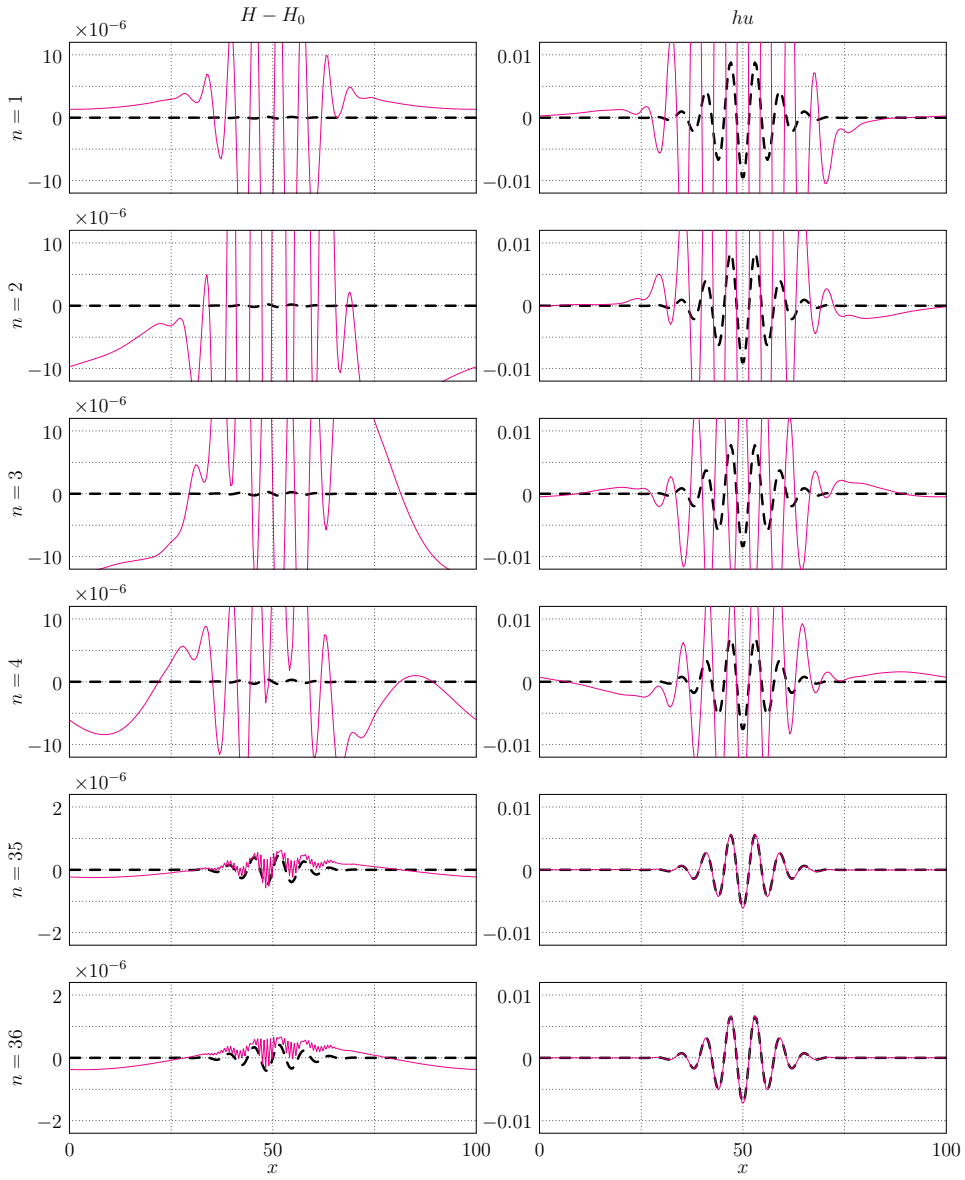

FIGURE 10. Same as Figure 9, but using the multiscale scheme (magenta).

6. Appendix

6.1. **Numerical fluxes of the finite volume scheme.** As outlined in (40), the numerical fluxes are computed in three steps. Here, the particular terms using the trapezoidal rule in the second correction are given. The case using the BDF(2) discretization uses the same spatial operators, but has some differences in the particular terms. $\mathbf{F}_I^*$ and $\mathbf{N}_i^*$ are the numerical fluxes approximating the flux function and "source term" of the auxiliary system, respectively. These are

$$\mathbf{F}_I^* = \begin{pmatrix} (hu)^{n+1/2} \\ (hu)^{n+1/2} u^{n+1/2} \end{pmatrix} \quad \text{and} \quad \mathbf{N}_i^* = \begin{pmatrix} 0 \\ -(hh'_x)^n \end{pmatrix} . \tag{61}$$

The second flux term

$$\mathbf{F}_I^{\mathsf{MAC}} \coloneqq -\frac{\Delta t}{2}\begin{pmatrix} h^n(\delta h_{\mathrm{fl}}'^{,n})_x \\ (hu)^{*,n+1/2}(\delta h_{\mathrm{fl}}'^{,n})_x + h^n(\delta h_{\mathrm{fl}}'^{,n})_x u^{*,n+1/2} \end{pmatrix}_I \tag{62}$$

corresponds to the first correction computed by equation (15). As stated above, with this correction the new time level fluid depth can be determined. The third contribution in (40) is given by

$$\mathbf{N}_i^{\mathsf{P2}} \coloneqq \begin{pmatrix} 0 \\ -\frac{1}{2}\left(\delta h^n h_x'^{,n} + h^{n+1/2}\delta h_x'^{,n}\right) \end{pmatrix}_i \tag{63}$$

and represents the correction computed by the second Helmholtz equation (19).

6.2. **"Simple wave" test case.** Computed errors and convergence rates (cf. section 4.2).

TABLE 1. Errors and convergence rates in h for the different variants of the semi-implicit method.

method	norm	256	rate γ	512	rate γ	1024	rate γ	2048
trapezoidal rule	L^2	3.2801e-3	1.846	9.1251e-4	1.955	2.3530e-4	1.991	5.9190e-5
	L^∞	1.0686e-2	1.705	3.2770e-3	1.898	8.7942e-4	1.977	2.2342e-4
BDF(2)	L^2	4.7937e-3	1.763	1.4127e-3	1.912	3.7548e-4	1.975	9.5495e-5
	L^∞	1.4599e-2	1.587	4.8593e-3	1.822	1.3743e-3	1.947	3.5642e-4
multiscale method	L^2	3.2793e-3	1.846	9.1193e-4	1.956	2.3512e-4	1.991	5.9157e-5
	L^∞	1.0661e-2	1.703	3.2748e-3	1.898	8.7882e-4	1.977	2.2328e-4

TABLE 2. Errors and convergence rates in (hu) for the different variants of the semi-implicit method.

method	norm	256	rate γ	512	rate γ	1024	rate γ	2048
trapezoidal rule	L^2	3.2422e-2	1.864	8.9047e-3	1.961	2.2875e-3	1.991	5.7556e-4
	L^∞	1.0527e-1	1.722	3.1899e-2	1.904	8.5226e-3	1.977	2.1654e-3
BDF(2)	L^2	4.7676e-2	1.740	1.4277e-2	1.910	3.8002e-3	1.976	9.6614e-4
	L^∞	1.4534e-1	1.573	4.8843e-2	1.826	1.3778e-2	1.952	3.5620e-3
multiscale method	L^2	3.2404e-2	1.865	8.8982e-3	1.961	2.2855e-3	1.990	5.7521e-4
	L^∞	1.0494e-1	1.720	3.1864e-2	1.904	8.5157e-3	1.976	2.1639e-3

Acknowledgements. R.K. acknowledges partial support by Deutsche Forschungsgemeinschaft through the collaborative research center CRC 1114 "Scaling cascades in complex systems", project A02. This work benefited greatly from free software products. Without these tools – such as LaTeX and the Linux operating system – a lot of tasks would not have been so easy to realize. It is our pleasure to thank all developers for their excellent products.

REFERENCES

[1] Peter R. Bannon. On the anelastic approximation for a compressible atmosphere. *Journal of the Atmospheric Sciences*, 53(23):3618–3628, 1996. doi:10.1175/1520-0469(1996)053<3618:OTAAFA>2.0.CO;2.

[2] François Bouchut. On zero pressure gas dynamics. In Benoît Perthame, editor, *Advances in kinetic theory and computing: selected papers*, volume 22 of *Series on Advances in Mathematics for Applied Sciences*, pages 171–190. World Scientific Publishing, 1994.

[3] François Bouchut, Shi Jin, and Xiantao Li. Numerical approximations of pressureless and isothermal gas dynamics. *SIAM Journal on Numerical Analysis*, 41(1):135–158, 2003. doi:10.1137/S0036142901398040.

[4] Didier Bresch, Rupert Klein, and Carine Lucas. Multiscale analyses for the shallow water equations. In Egon Krause, Yurii Shokin, Michael Resch, Dietmar Kröner, and Nina Shokina, editors, *Computational Science and High Performance Computing IV*, volume 115 of *Notes on Numerical Fluid Mechanics and Multidisciplinary Design*, pages 149–164. Springer Berlin / Heidelberg, 2011. ISBN 978-3-642-17769-9. doi:10.1007/978-3-642-17770-5_12.

[5] Floraine Cordier, Pierre Degond, and Anela Kumbaro. An asymptotic-preserving all-speed scheme for the Euler and Navier-Stokes equations. *Journal of Computational Physics*, 231(17):5685–5704, 2012. doi:10.1016/j.jcp.2012.04.025.

[6] Richard Courant, Kurt Otto Friedrichs, and Hans Lewy. Über die partiellen Differenzengleichungen der mathematischen Physik. *Mathematische Annalen*, 100:32–74, 1928. doi:10.1007/BF01448839.

[7] Terry Davies, Andrew Staniforth, Nigel Wood, and John Thuburn. Validity of anelastic and other equation sets as inferred from normal-mode analysis. *Quarterly Journal of the Royal Meteorological Society*, 129(593):2761–2775, 2003. doi:10.1256/qj.02.1951.

[8] Peter Deuflhard and Folkmar Bornemann. *Scientific Computing with Ordinary Differential Equations*, volume 42 of *Texts in Applied Mathematics*. Springer, 2002.

[9] Dale R. Durran. Improving the anelastic approximation. *Journal of the Atmospheric Sciences*, 46(11):1453–1461, 1989. doi:10.1175/1520-0469(1989)046<1453:ITAA>2.0.CO;2.

[10] Gerhard Erbes. A semi-lagrangian method of characteristics for the shallow-water equations. *Monthly Weather Review*, 121(12):3443–3452, 1993. doi:10.1175/1520-0493(1993)121<3443:ASLMOC>2.0.CO;2.

[11] Karl Josef Geratz. *Erweiterung eines Godunov-Typ-Verfahrens für zweidimensionale kompressible Strömungen auf die Fälle kleiner und verschwindender Machzahl*. PhD dissertation, Rheinisch-Westfälische Technische Hochschule Aachen, 1997.

[12] Sigal Gottlieb, Chi-Wang Shu, and Eitan Tadmor. Strong stability-preserving high-order time discretization methods. *SIAM Review*, 43(1):89–112, 2001. doi:10.1137/S003614450036757X.

[13] Francis H. Harlow and J. Eddie Welch. Numerical calculation of time-dependent viscous incompressible flow of fluid with free surface. *The Physics of Fluids*, 8 (12):2182–2189, 1965. doi:10.1063/1.1761178.

[14] Eugenia Kalnay. *Atmospheric Modeling, Data Assimilation and Predictability*. Cambridge University Press, 2003.

[15] Jirair Kevorkian and Julian D. Cole. *Multiple Scale and Singular Perturbation Methods*, volume 114 of *Applied Mathematical Sciences*. Springer, New York, 1996.

[16] Sergiu Klainerman and Andrew Majda. Singular limits of quasilinear hyperbolic systems with large parameters and the incompressible limit of compressible fluids. *Communications in Pure Applied Mathematics*, 34(4):481–524, 1981. doi:10.1002/cpa.3160340405.

[17] R. Klein and T. Benacchio. A doubly blended model for multiscale atmospheric dynamics. *J. Atmos. Sci.*, 73:1179–1186, 2016.

[18] Rupert Klein. Semi-implicit extension of a Godunov-Type scheme based on low Mach number asymptotics I: One-dimensional flow. *Journal of Computational*

Physics, 121:213–237, 1995. doi:10.1016/S0021-9991(95)90034-9.

[19] Rupert Klein. Asymptotic analyses for atmospheric flows and the construction of asymptotically adaptive numerical methods. *Zeitschrift für Angewandte Mathematik und Mechanik*, 80(11-12):765–777, 2000.

[20] Rupert Klein. An applied mathematical view of meteorological modelling. In James M. Hill and Ross Moore, editors, *Applied Mathematics Entering the 21st Century: Invited talks from the ICIAM 2003 Congress*, volume 116 of *Proceedings in Applied Mathematics*, pages 227–269, 2004.

[21] Rupert Klein. Asymptotics, structure, and integration of sound-proof atmospheric flow equations. *Theoretical and Computational Fluid Dynamics*, 23: 161–195, 2009. doi:10.1007/s00162-009-0104-y.

[22] Rupert Klein. Scale-dependent models for atmospheric flows. *Annual Review of Fluid Mechanics*, 42:249–274, 2010. doi:10.1146/annurev-fluid-121108-145537.

[23] Rupert Klein, Nicola Botta, Thomas Schneider, Claus-Dieter Munz, Sabine Roller, Andreas Meister, L. Hoffmann, and Thomas Sonar. Asymptotic adaptive methods for multi-scale problems in fluid mechanics. *Journal of Engineering Mathematics*, 39(1):261–343, 2001. doi:10.1023/A:1004844002437.

[24] Rupert Klein, Stefan Vater, Eileen Päschke, and Daniel Ruprecht. Multiple scales methods in meteorology. In Herbert Steinrück, editor, *Asymptotic Methods in Fluid Mechanics: Survey and Recent Advances*, volume 523 of *CISM International Centre for Mechanical Sciences*, pages 127–196. Springer, 2011. URL `http://www.springer.com/materials/mechanics/book/978-3-7091-0407-1`.

[25] Olivier Le Maître, Julia Levin, Mohamed Iskandarani, and Omar M. Knio. A multiscale pressure splitting of the shallow-water equations i. formulation and 1d tests. *Journal of Computational Physics*, 166(1):116–151, 2001. doi:10.1006/jcph.2001.6647.

[26] Randall J. LeVeque. The dynamics of pressureless dust clouds and delta waves. *Journal of Hyperbolic Differential Equations*, 1(2):315–327, 2004. doi:10.1142/S0219891604000135.

[27] Franik B. Lipps and Richard S. Hemler. A scale analysis of deep moist convection and some related numerical calculations. *Journal of the Atmospheric Sciences*, 39(10):2192–2210, 1982. doi:10.1175/1520-0469(1982)039<2192:ASAODM>2.0.CO;2.

[28] Andrew J. Majda and Rupert Klein. Systematic multiscale models for the tropics. *Journal of the Atmospheric Sciences*, 60(2):393–408, 2003. doi:10.1175/1520-0469(2003)060<0393:SMMFTT>2.0.CO;2.

[29] Claus-Dieter Munz, Sabine Roller, Rupert Klein, and Karl Josef Geratz. The extension of incompressible flow solvers to the weakly compressible regime. *Computers & Fluids*, 32(2):173–196, 2003.

[30] Yoshimitsu Ogura and Norman A. Phillips. Scale analysis of deep and shallow convection in the atmosphere. *Journal of the Atmospheric Sciences*, 19(2): 173–179, 1962. doi:10.1175/1520-0469(1962)019<0173:SAODAS>2.0.CO;2.

[31] W. Ohfuchi, H. Nakamura, M.K. Yoshioka, T. Enomoto, K. Takaya, X. Peng, S. Yamane, T. Nishimura, Y. Kurihara, and K. Ninomiya. 10-km mesh mesoscale resolving simulations of the global atmosphere on the Earth Simulator: Preliminary outcomes of AFES (AGCM for the Earth Simulator). *Journal of the Earth Simulator*, 1:8–34, 2004.

[32] Stanley Osher. Convergence of generalized MUSCL schemes. *SIAM Journal on Numerical Analysis*, 22(5):947–961, 1985. doi:10.1137/0722057.

[33] Joseph Pedlosky. *Geophysical Fluid Dynamics*. Springer, New York, 2 edition, 1987.

[34] Chi-Wang Shu and Stanley Osher. Efficient implementation of essentially non-oscillatory shock-capturing schemes. *Journal of Computational Physics*, 77 (2):439–471, 1988. ISSN 0021-9991. doi:10.1016/0021-9991(88)90177-5.

[35] Endre Süli. Convergence of finite volume schemes for Poisson's equation on nonuniform meshes. *SIAM Journal on Numerical Analysis*, 28(5):1419–1430, 1991. ISSN 0036-1429. doi:10.1137/0728073.

[36] U. Trottenberg, C.W. Oosterlee, and A. Schüller. *Multigrid*. Academic Press, 2001. ISBN 0-12-701070-X.

[37] Geoffrey K. Vallis. *Atmospheric and Oceanic Fluid Dynamics*. Cambridge University Press, Cambridge, U.K., 2006.

[38] Henk A. van der Vorst. Bi-CGSTAB: A fast and smoothly converging variant of Bi-CG for the solution of nonsymmetric linear systems. *SIAM Journal on Scientific and Statistical Computing*, 13(2):631–644, 1992. doi:10.1137/0913035.

[39] Bram van Leer. Towards the ultimate conservative difference scheme. V. A second-order sequel to Godunov's method. *Journal of Computational Physics*, 32(1):101–136, 1979. doi:10.1016/0021-9991(79)90145-1.

[40] Stefan Vater. *A Multigrid-based Multiscale Numerical Scheme for Shallow Water Flows at Low Froude Number*. PhD thesis, Freie Universität Berlin, 2013. URL `http://www.diss.fu-berlin.de/diss/receive/FUDISS_thesis_000000093897`.

[41] Stefan Vater and Rupert Klein. Stability of a Cartesian grid projection method for zero Froude number shallow water flows. *Numerische Mathematik*, 113(1): 123–161, 2009. doi:10.1007/s00211-009-0224-8.

[42] Stefan Vater, Rupert Klein, and Omar M. Knio. A scale-selective multilevel method for long-wave linear acoustics. *Acta Geophysica*, 59(6):1076–1108, 2011. doi:10.2478/s11600-011-0037-x.

[43] J. Eddie Welch, Francis H. Harlow, J. P. Shannon, and B. J. Daly. The mac method - a computing technique for solving viscous, incompressible, transient fluid-flow problems involving free surfaces. Technical Report LA-3425, Los Alamos Scientific Laboratory, 1965.

Stefan Vater: `stefan.vater@uni-hamburg.de`
Department of Mathematics / Center for Earth System Research and Sustainability (CEN), Universität Hamburg, Bundesstraße 55, 20146 Hamburg, Germany

Rupert Klein: `rupert.klein@math.fu-berlin.de`
Department of Mathematics and Computer Science, Freie Universität Berlin, Arnimallee 14, 14195 Berlin, Germany